Contributions to Mineralogy and Petrology (2020) 175:34
https://doi.org/10.1007/s00410-020-1671-6

ORIGINAL PAPER

Unravelling the processes controlling apatite formation in the Phalaborwa Complex (South Africa) based on combined cathodoluminescence, LA-ICPMS and in-situ O and Sr isotope analyses

Sophie Decrée[1] · Grant Cawthorn[2] · Etienne Deloule[3] · Julien Mercadier[4] · Hartwig Frimmel[5] · Jean-Marc Baele[6]

Received: 17 November 2019 / Accepted: 6 March 2020 / Published online: 23 March 2020

Abstract

The Phalaborwa world-class phosphate deposit (South Africa) is hosted by a Paleoproterozoic alkaline complex mainly composed of phoscorite, carbonatite, pyroxenitic rocks, and subordinate fenite. In addition, syenite and trachyte occur in numerous satellite bodies. New petrological and in-situ geochemical data along with O and Sr isotope data obtained on apatite demonstrate that apatite is in the principal host rocks (pyroxenitic rocks, phoscorite and carbonatite) formed primarily by igneous processes from mantle-derived carbonatitic magmas. Early-formed magmatic apatite is particularly enriched in light rare earth elements (LREE), with a decrease in the REE content ascribed to magma differentiation and early apatite fractionation in isolated interstitial melt pockets. Rayleigh fractionation favored a slight increase in $\delta^{18}O$ (below 1%) at a constant Sr isotopic composition. Intrusion of fresh carbonatitic magma into earlier-formed carbonatite bodies locally induced re-equilibration of early apatite with REE enrichment but at constant O and Sr isotopic compositions. In fenite, syenite and trachyte, apatite displays alteration textures and LREE depletion, reflecting interaction with fluids. A marked decrease in $\delta^{18}O$ in apatite from syenite and trachyte indicates a contribution from $\delta^{18}O$-depleted meteoric fluids. This is consistent with the epizonal emplacement of the satellite bodies. The general increase of the Sr isotope ratios in apatite in these rocks reflects progressive interaction with the country rocks over time. This study made it possible to decipher, with unmatched precision, the succession of geological processes that led to one of the most important phosphate deposits worldwide.

Keywords Carbonatite-related ore deposits · Kaapvaal craton · Paleoproterozoic · Rare earth elements · Sr and O isotopes

Communicated by Daniela Rubatto.

Electronic supplementary material The online version of this article (https://doi.org/10.1007/s00410-020-1671-6) contains supplementary material, which is available to authorized users.

✉ Sophie Decrée
sophie.decree@naturalsciences.be

Grant Cawthorn
grant.cawthorn@wits.ac.za

Etienne Deloule
etienne.deloule@univ-lorraine.fr

Julien Mercadier
julien.mercadier@univ-lorraine.fr

Hartwig Frimmel
hartwig.frimmel@uni-wuerzburg.de

Jean-Marc Baele
jean-marc.baele@umons.ac.be

[1] Royal Belgian Institute of Natural Sciences-Geological Survey of Belgium, Brussels, Belgium

[2] School of Geosciences, University of the Witwatersrand, PO Wits, Johannesburg 2050, South Africa

[3] CRPG, UMR 7358, CNRS-Université de Lorraine, Vandœuvre-lès-Nancy, France

[4] Université de Lorraine, CNRS, CREGU, GeoRessources Lab, Vandoeuvre-lès-Nancy, France

[5] Bavarian Georesources Centre, Department of Geodynamics and Geomaterials Research, Institute of Geography and Geology, University of Würzburg, Würzburg, Germany

[6] Department of Geology and Applied Geology, University of Mons, Mons, Belgium

Introduction

Alkaline complexes and related carbonatites are of interest because of their high economic potential, with associated strategic resources of rare earth elements (REE) and niobium (Deans 1966; Mariano 1989; Pell 1996). Phosphate (as apatite) is one of the main commodities mined from these rocks. Recent studies have highlighted that phosphate deposits represent a potential source of REE, which could resolve part of the world's supply shortage of REE (e.g. Ihlen et al. 2014; Emsbo et al. 2015; Goodenough et al. 2016). Magmatic apatite usually contains more than 0.35% REE, with low contents of unwanted contaminants (Ihlen et al. 2014). Moreover, extraction of REE from phosphate deposits is relatively easy and is less harmful to the environment compared to traditional REE prospects (Emsbo et al. 2015).

Apatite associated with carbonatites and alkaline complexes can be accumulated-locally into economic quantities by various processes ranging from magmatic, late-magmatic, metasomatic and hydrothermal processes or supergene alteration (e.g. Broom-Fendley et al. 2016a; Decrée et al. 2016; De Toledo et al. 2004; Giebel et al. 2017; Vartiainen and Paarma 1979; Walter et al. 1995). Apatite formed in carbonatites and alkaline complexes is typically enriched in REE. This enrichment is dependent on the processes leading to apatite formation; hence, our interest is in deciphering these processes. However, due to possible spatial superimposition of the various phosphate-forming processes over time, the assessment of the relative importance of each individual genetic process is not straightforward. The objective of this work is, therefore, to tackle this question by studying apatite using a wide range of in-situ techniques.

The case study investigated here is the world-class phosphate deposit of Phalaborwa, located in the Archean Kaapvaal Craton of South Africa (Eriksson 1989). The Phalaborwa deposit is related to an alkaline and carbonatitic complex dated at 2060 ± 2 Ma (Reischmann 1995; Wu et al. 2011). The pipe-shaped deposit and associated satellite intrusions mainly comprise pyroxenites, with subordinate phoscorite and carbonatite (Fig. 1). Most of the phosphate at Phalaborwa occurs as apatite in phoscorite, but there are also large reserves of pyroxenite. Remaining resources are considerable, estimated at 18,370 Mt of ore (averaging 7 wt% P_2O_5; Orris and Chernoff 2002). Other commodities are iron, copper, gold, platinum group elements and uranium (e.g. Rudashevsky et al. 2004). The Phalaborwa deposit also offers a potential for recovering REE, with estimated resources of 652 Mt at 0.15% total REE oxides (Jackson and Christiansen 1993). The average total REE oxide content is about 6000 ppm in phoscorite-derived concentrates, and ~ 8000 ppm in carbonatite- and pyroxenite-derived apatite concentrates (Buchholz and Foya 2015).

Previous studies on apatite composition by Dawson and Hinton (2003), Wu et al. (2011) and Milani et al. (2017) provided clues about element partitioning, magmatic evolution and element sourcing at Phalaborwa. Among others, these authors argued for a common genetic origin of the phoscorite–carbonatite assemblage. Giebel et al. (2017, 2019) highlighted the involvement of late- to post-magmatic fluids in the mobilization, and the possible introduction of REE into the mineralizing system. Although these studies constitute important steps in the understanding of magmatic to post-magmatic processes in the Phalaborwa Complex, only phoscorite and carbonatite have been investigated. To better constrain the succession of processes in the apatite genesis and associated REE enrichment, this study presents a detailed petrographic and geochemical investigation of apatite from a wide variety of lithotypes at Phalaborwa, including those containing the highest apatite contents, such as the apatite veins that crosscut the complex.

Petrographic observations under cathodoluminescence (CL) were performed to reveal chemical zonation in apatite. As chemical heterogeneity of apatite can occur on a very small-scale, chemical and isotopic variations were measured by in-situ methods. Electron microprobe analyses (EMPA) and laser ablation-inductively coupled plasma mass spectrometry (LA-ICPMS) were used to quantify the chemical composition, from major to trace elements (including REEs), whereas the oxygen and strontium isotopic compositions were determined by secondary ion mass spectrometry (SIMS). In-situ isotopic investigations have been, however, rare so far (e.g. Emo et al. 2018; Li et al. 2018; Yang et al. 2018; Zeng et al. 2016; Zhao et al. 2015 for Sr isotope composition, and Chen et al. 2016; Sun et al. 2016; Zeng et al. 2016; and Zigaitė and Whitehouse 2014 for O isotope compositions), and very few are related to apatite in the context of alkaline magmatism (Wu et al. 2011). This work presents a novel approach combining high spatial resolution O and Sr analyses, aiming at deciphering, with unmatched precision, the processes involved in apatite formation. This approach is of broad interest in a large range of geological settings. In the present case, the application of such a methodology can give unique insights into the processes and source(s) involved in the origin of phosphate deposits associated with alkaline complexes and carbonatites (e.g. Broom-Fendley et al. 2016a; Conway and Taylor 1969; Santos and Clayton 1995; Tichomirowa et al. 2006; Wu et al. 2011). Only few O isotope compositions have been, for example, obtained in Phalaborwa (13 in total, mostly of carbonatite; Pineau et al. 1973; Suwa et al. 1975; Eriksson 1982, 1989). The data acquired in the framework of this study thus significantly increase the dataset available for the Phalaborwa Complex. A further motivation for this study comes from the high potential of such deposits for future REE recovery.

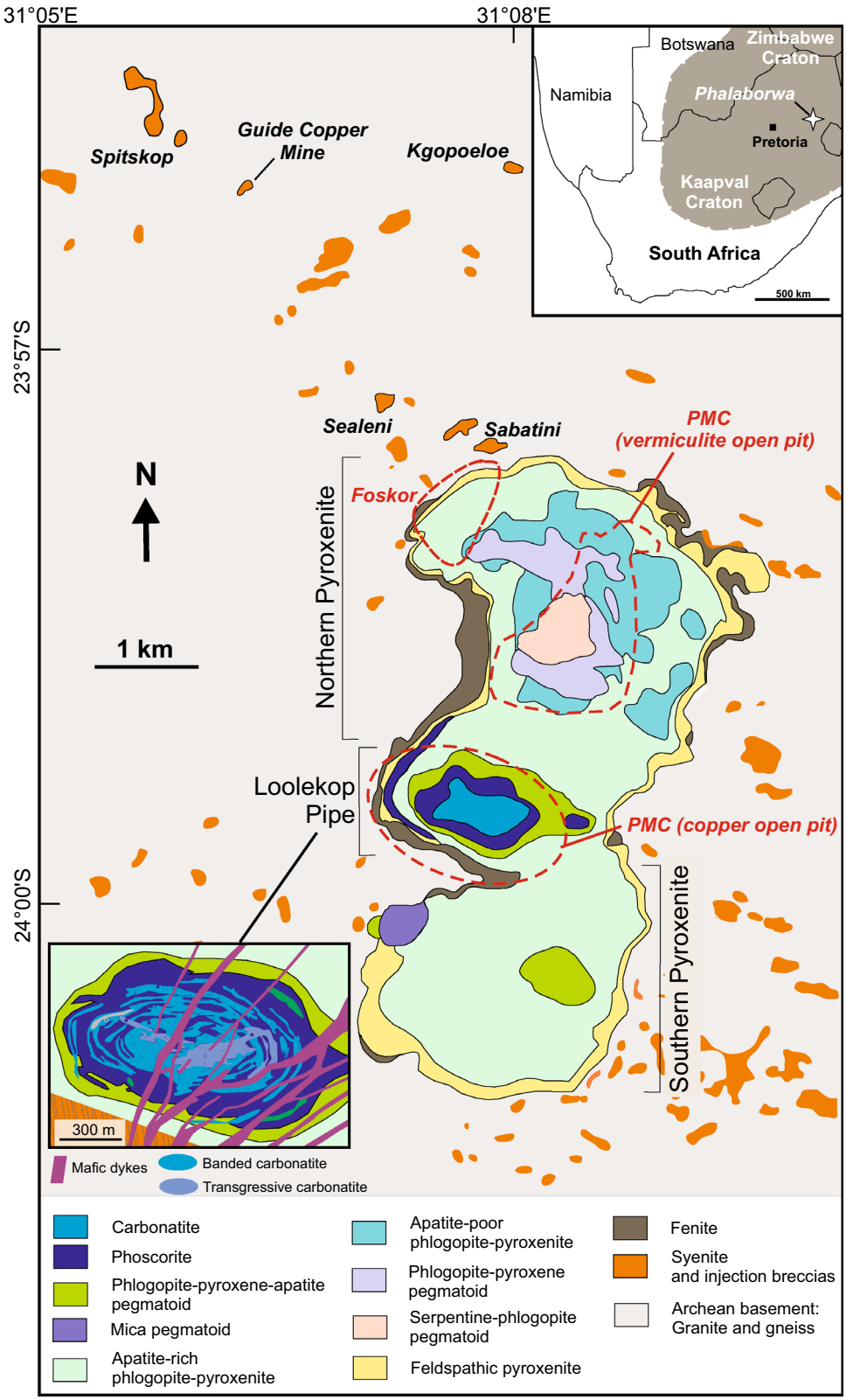

Fig. 1 Geological sketch map of the Phalaborwa Complex (modified and redrawn from Hanekom (1965) (in Eriksson 1982) and de Jager (1989). The upper insert shows the location of Phalaborwa in South Africa and in the Kaapvaal Craton. The lower insert illustrates the detailed geology of the Loolekop carbonatite pipe (modified from Verwoerd and Du Toit 2006)

Geological context

The pipe-shaped 2060 ± 2 Ma Phalaborwa Complex is located about 350 km to the NE of Pretoria (South Africa). It was emplaced into Archean basement rocks comprising of granitoids, gneisses, amphibolites, and talc–serpentinite schists (Groves and Vielreicher 2001). The intrusive complex is about 6.5 km long and 1.5–3.5 km wide. It comprises three lobes called Northern Pyroxenite, Loolekop, and Southern Pyroxenite (Fig. 1). These lobes coalesce to form the main body of the complex. The contacts and mineral banding in the complex are mostly vertical, with its main features and mineralization having been drilled to a depth of > 1000 m, though the full extent of the deposit at depth remains unknown (Roux et al. 1989).

Pyroxenitic rocks, phoscorite and carbonatite are the most abundant rock types at Phalaborwa (Fig. 2a–f). Clinopyroxenites constitute about 70% volume of the complex. They grade from massive pyroxenite to glimmerite (a rock mainly made of phlogopite; Eriksson 1989). The division between micaceous pyroxenite and massive clinopyroxenite is based on the modal proportion of clinopyroxene and phlogopite (Eriksson 1982), with the latter having been interpreted as a hydrothermal or metasomatic mineral related to the emplacement of the pyroxenite (Fourie and de Jager 1986;

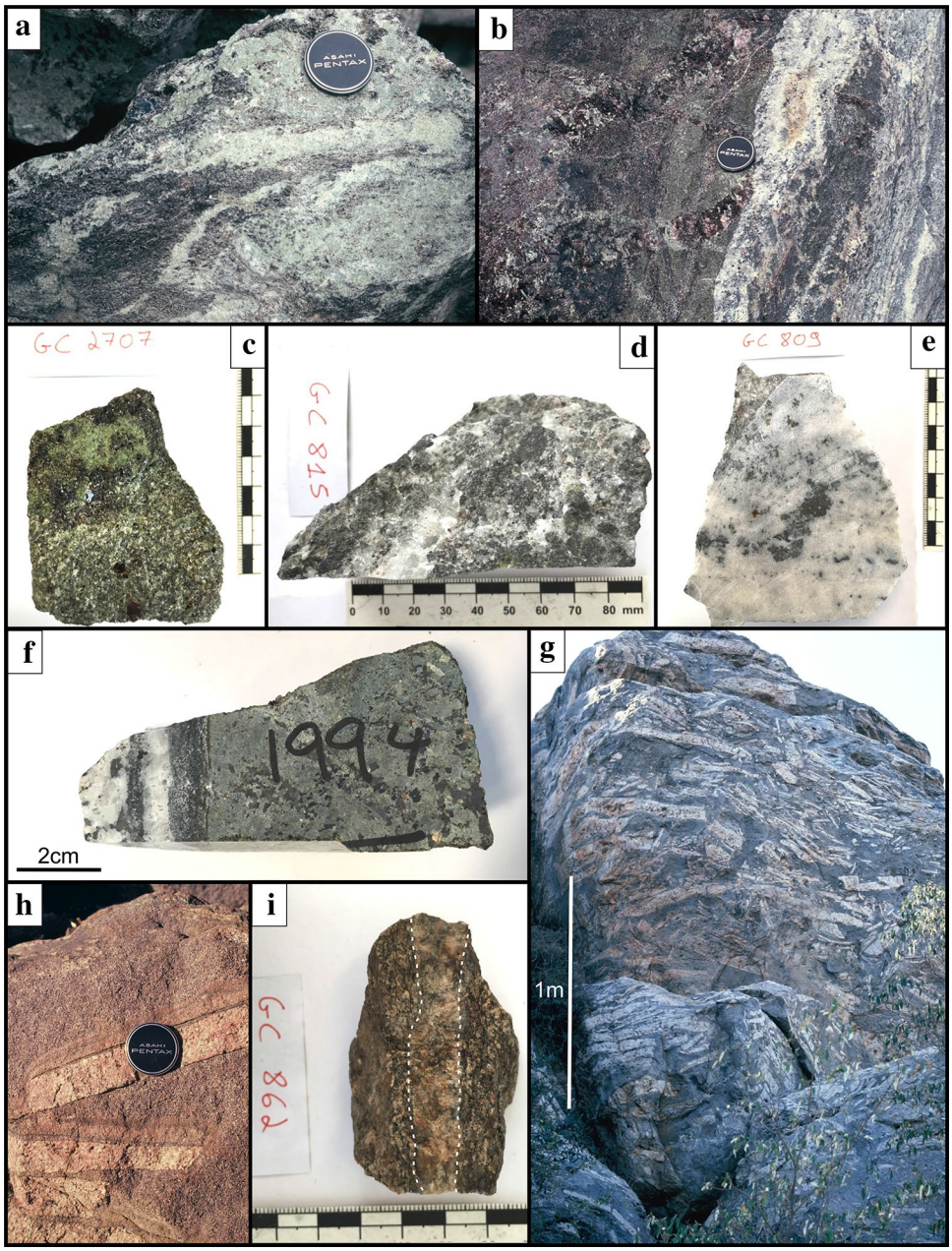

Fig. 2 Selected field pictures (**a**, **b**, **h**, **g**) and macrophotographs (**c**, **d**, **e**, **f**, **i**) of Phalaborwa rocks. **a** Diffused veins of apatite in heterogeneous mica-pyroxene rock (Foskor); **b** carbonatite cutting pegmatitic pyroxenite (Foskor); **c** micaceous pyroxenite (apatite-mica-cpx rock) with fragments of mica (sample GC 2707, Foskor); **d** phoscorite (sample GC 815, PMC); **e** banded carbonatite (sample GC 809, PMC); **f** banded carbonatite cutting a pyroxenitic rock (sample GC 1994, Foskor); **g** slabby syenite breccia at Kgopoeloe; **h** slabby breccia of coarse syenite in microsyenite (Kgopoeloe); **i** trachyte dikelet cutting fenite (sample GC 862, Spitskop)

Lombaard et al. 1964). A recent study by Giebel et al. (2019) emphasizes, however, that phlogopite is an orthomagmatic phase, whereas tetraferriphlogopite is related to late-magmatic to hydrothermal processes, which also introduced REE in the Phalaborwa deposit. A general positive correlation is observed between apatite and phlogopite content (Fourie and de Jager 1986). Pegmatoid dikes made of phlogopite, apatite and diopside occur in the Northern and Southern pyroxenites (Eriksson 1982). This pyroxenite pegmatoid could be related to intense metasomatism (Wu et al. 2011). Apatite-rich pegmatoid dikes and veins (Fig. 2a) have a wider distribution and are younger than all the pyroxenitic rocks (Fourie and de Jager 1986) and are, in turn, cut by syenite dikes (de Jager 1989; Heinrich 1970).

Feldspathic pyroxenite is developed in close contact with country rocks and where pyroxenite occurs in association with the younger syenite. In many places, it grades into massive pyroxenite, even though contacts are locally sharp (Eriksson 1982). The feldspathic pyroxenite has a magmatic and not metasomatic origin, and its Sr isotope composition is similar to that of clinopyroxenite in the complex (Eriksson 1989).

Phoscorite consists of olivine, apatite and magnetite (Eriksson 1982). Irregular patches and lenses of carbonatite within phoscorite become larger and more abundant towards the inner part of the intrusive complex, ending in the carbonatite body (Eriksson 1982). Two types of carbonatite are encountered in the complex, i.e. a banded and a transgressive carbonatite. The banded carbonatite occurs in the center of the phoscorite (Eriksson 1989), with which it has both sharp and gradational contacts (Wu et al. 2011). Several episodes of remobilization of banded carbonatite are evident (Eriksson 1989). The different generations are similar in mineralogy and texture, have comparatively low Mg contents ($\leq$7.5 wt% $MgCO_3$; Lombaard et al. 1964 in Eriksson 1982) and exsolution lamellae of dolomite (Eriksson 1989). The transgressive carbonatite is localized in the inner part of the central intrusive body and radiates from it along fractures (Eriksson 1989). In contrast, the transgressive carbonatite is enriched in Mg (up to 14 wt% of $MgCO_3$; Hennig-Michaeli 1968 in Eriksson 1982).

Magmatic crystallization of apatite, clinopyroxene, and phlogopite has been regarded as the main process forming the Phalaborwa Complex (Eriksson 1989), through mixing of magma batches with distinct compositions (Milani et al. 2017). Pyroxenites are thought to have been derived from a potassic ultrabasic liquid during the initial stage of emplacement and developed independently from phoscorite and carbonatites. This first period of intrusion was followed by the injection of a silica-poor carbonate-rich magma forming the banded carbonatite and the phoscorite (Eriksson 1982). Mineralogical and geochemical studies suggest that phoscorite and carbonatite originated from a common parental magma that is unmixed (e.g. Giebel et al. 2019). Fracturing and renewed magmatic activity in the central (Loolekop) body led to the formation of the transgressive carbonatites (Eriksson 1982; Wu et al. 2011). The parental magma for most of the Phalaborwa rocks was derived from a metasomatised enriched lithospheric mantle (Wu et al. 2011). Metasomatism in the main complex is limited to fenitization of country rocks, and formation of minor phlogopite in phoscorite and carbonatite (Eriksson 1982).

Satellite bodies (namely Guide Copper Mine, Spitskop and Kgopoeloe) occur at a distance of up to 4–5 km from the main complex (Fig. 1). They comprise of feldspathic pyroxenite, peralkaline (quartz) syenite, peralkaline granite and trachyte (Eriksson 1989; Fig. 2g–i). Their chemistry suggests that their parental magma interacted with country rocks, with a greater degree of differentiation than in the main body (Eriksson 1989). Kgopoeloe is a breccia plug of about 150 m in diameter that resulted from explosive processes (Fig. 2g, h). It mostly consists of granitic clasts in a syenitic matrix. The brecciation is related to fluids derived from the syenite (Eriksson 1982). Spitskop comprises a ring syenite of about 300 m diameter that encloses a central syenite, which is cut by dikes of finer-grained syenite and trachyte. There are few indications of brecciation at Spitskop. Consequently, Kgopeloe would represent the highest structural level, whereas Spitskop represents a lower level (Eriksson 1982).

The feldspathic pyroxenite of the Guide Copper Mine has been interpreted to be cogenetic with the pyroxenites of the main complex. The satellite bodies have been variously interpreted as unrelated to the main complex (Eriksson 1982), or the result of differentiation of magma related to the main complex (Frick 1975).

Materials and methods

Thirty samples were taken from Foskor, PMC mine, Sabatini, Sealeni, Guide Copper Mine, Spitskop and Kgopoeloe (Fig. 1; Table 1). Petrographic analysis was based on optical microscopy and scanning electron microscopy (SEM) using a Quanta 20 ESEM (FEI), with energy-dispersive spectroscopy (Apollo 10 Sillicon Drift EDS detector; EDAX) at the Royal Belgian Institute of Natural Sciences. Cathodoluminescence (CL) studies were performed at the University of Mons using a cold-cathode CL unit model Mk5 operated at 15 kV beam voltage and 500 µA current (Cambridge Image Technology Limited). The surface of the unfocused electron beam on the sample was 12 × 4 mm, resulting in a current density of about 10 µA/mm^2. CL spectra were recorded with a CITL optical spectrometer model

Table 1 Succinct description of all examined samples from the Phalaborwa Complex. The rocks mentioned in this paper are in bold and italic

Sample	Description	Location
GC 368	Syenite cutting pyroxenite	Foskor
GC 610	Phoscorite	PMC
GC 809	**Banded carbonatite**	**PMC**
GC 810	Sulfide-rich carbonatite	PMC
GC811	**Magnetite-rich banded carbonatite**	**PMC**
GC813	Carbonatites cutting phoscorite	PMC
GC 814	**Phoscorite-carbonatite contact**	**PMC**
GC 815	**Phoscorite**	**PMC**
GC 816	Phoscorite	PMC
GC 826	Micaceous pyroxenite/layered cpx-mica rock	Foskor
GC 828	**Fenite breccia**	**Sealeni**
GC 832	**Syenite**	**Kgopolwe**
GC 835	Syenite-pyroxenite contact	Spitskop
GC 836	Syenite	Spitskop
GC 862	**Trachyte cutting fenite**	**Spitskop**
GC 865	Contact pyroxenite with cpx-ap-mica pegmatite	Foskor
GC 1524	**Feldspathic pyroxenite**	**Guide copper mine**
GC 1609	Apatite-rich rock	PMC
GC 1992	Cpx-mica pegmatite	Foskor
GC 1994	**Banded carbonatite cutting pyroxenite**	**Foskor**
GC 2701	**Apatite with clots of mica**	**Foskor**
GC 2702	**Apatite vein cutting glimmerite**	**Foskor**
GC 2703	Apatite vein cutting glimmerite	Foskor
GC 2704	**Micaceous pyroxenite/apatite-mica rock**	**Foskor**
GC 2704 BIS	Micaceous pyroxenite/apatite-mica rock	Foskor
GC 2705	**Apatite vein**	**Foskor**
GC 2706	**Pyroxenite at edge of syenite**	**Foskor**
GC 2707	**Micaceous pyroxenite/apatite-mica-cpx rock with fragments of mica**	**Foskor**
SB1	Syenite	Sabatini
SB13	Pyroxenite	Sabatini

OSA2 allowing acquisition from 350 to 1100 nm at 3.7 nm spectral resolution. Spectra were acquired and processed using Spectragryph optical spectroscopy software (https://www.effemm2.de/spectragryph/). Spectral CL images of the Nd^{3+} emission were collected by inserting in the light path an optical bandpass filter with a transmission curve centered at 880 nm and 50 nm wide (full width at half maximum). Such spectral CL imaging enhances the details of the distribution of the apatite activated by light REE, which is especially useful when apatite luminescence is overwhelmed by the intense luminescence of calcite and feldspars. In addition, Nd^{3+} emits in the near infrared region of the spectrum and is therefore not visible in color CL images.

Among the 30 samples investigated petrographically, 13 representative ones were selected for further in-situ geochemical analyses in zoned apatite. Where possible, the different types of analyses (EMPA, LA-ICPMS and SIMS) have been performed on the same spot or nearby. These analytical spots are referred to in Tables 2, 3, 4 and the location of most of these spots is indicated on Figs. 2,3, 4. Quantitative microanalyses of the chemical composition for major elements (Table 2) were acquired using a JEOL JXA 8800L electron microprobe at the Institute of Geography and Geology, University of Würzburg (Germany). It was operated at 15 kV and 20 nA, with a beam diameter of 10 µm. This microprobe is equipped with four wavelength-dispersive (WDS) spectrometers and standard LDE1, TAP, PET and LIF crystals (LiF for F, Fe_2O_3 for Fe, $SrSO_4$ for Sr, $MnTiO_3$ for Mn, MgO for Mg, $BaSO_4$ for S and Ba) and mineral standards (albite for Na, vanadinite for Cl, apatite for P and Ca, and andradite for Si) supplied by CAMECA (SX Geo-Standards) were used for reference. The Lα line was used for the measurements of Sr and Ba, and the Kα line for all other elements. The lower limit of detection is typically better than 0.05 wt%. For each mineral spot, the relatively mobile elements F and Na were analyzed for first to prevent

Table 2 Representative microprobe analyses (oxides in wt. %) of apatite from the Phalaborwa Complex

												Pyroxenitic rocks									
	Phoscorite					Carbonatite						Massive pyroxenite				Micaceous pyroxenite					
Sample	GC 814			GC 815		GC 814			GC 1994			GC 1994		GC 2706		GC 2704		GC 2707			
Analysis spot	7B-1	7B-2	7B-6	8–2	8–5	7A-1	7A-2	7A-3	22A-1	22A-4	22A-5	22C-1	22C-2	29–2	29–4	26A-2	26A-3	30–1	30–2	30–3	30–4
F[a]	2.70	2.60	2.80	2.56	3.12	2.62	2.75	2.70	3.11	3.33	3.25	3.20	2.66	2.58	3.00	2.76	2.57	2.80	2.61	2.81	2.29
Cl	–	–	–	–	–	–	–	–	–	0.05	0.06	0.09	0.07	–	0.05	–	–	–	–	–	–
SO_3	0.07	–	–	–	–	–	0.05	–	–	–	–	–	–	–	–	–	–	–	–	–	0.06
SiO_2	0.12	0.07	0.05	0.07	0.12	0.19	0.11	0.22	0.14	0.17	0.16	0.52	0.46	0.25	0.15	0.17	0.40	0.16	–	0.40	0.43
P_2O_5	40.28	40.84	40.58	38.32	38.12	40.94	40.50	40.33	40.00	39.18	41.44	40.14	39.42	39.69	41.19	39.76	40.60	41.11	39.80	40.49	39.77
FeO	0.06	–	–	0.24	–	–	–	–	–	0.13	0.05	–	–	–	0.11	0.09	0.05	0.22	0.07	0.14	–
MnO	–	–	–	0.05	0.08	–	–	–	–	–	0.12	–	–	–	0.07	–	–	–	0.13	–	–
MgO	–	–	0.08	–	–	–	–	–	–	–	–	–	–	–	–	–	–	–	–	–	–
Na_2O	–	0.05	0.07	0.15	0.11	–	0.15	–	0.14	0.06	0.12	0.11	0.14	0.09	0.08	0.08	0.12	–	–	–	–
BaO	–	–	0.06	–	–	–	0.11	–	–	0.07	–	0.09	–	–	–	–	–	–	–	–	–
SrO	–	0.53	0.56	0.35	0.44	0.34	0.40	0.28	0.64	0.53	0.52	0.73	0.68	0.70	0.73	0.67	0.61	0.72	0.73	0.68	0.67
CaO	54.27	54.86	55.48	55.56	54.00	55.20	55.12	54.99	54.31	55.17	55.48	53.18	53.78	54.49	55.59	55.27	53.38	53.06	55.52	54.87	54.58
O=F,Cl	1.14	1.09	1.18	1.07	1.32	1.10	1.16	1.14	1.31	1.41	1.38	1.36	1.13	1.09	1.27	1.17	1.08	1.18	1.10	1.18	0.97
Total	96.90	97.92	98.53	96.26	94.80	98.30	98.05	97.46	97.09	97.27	99.86	96.78	96.12	96.79	99.72	97.67	96.72	96.98	97.84	98.21	96.95
F	0.741	0.704	0.758	0.714	0.886	0.707	0.746	0.737	0.855	0.921	0.866	0.879	0.737	0.712	0.803	0.756	0.702	0.764	0.715	0.762	0.627
Cl	0.005	0.002	0.000	0.000	0.007	0.003	0.004	0.005	0.006	0.007	0.009	0.014	0.010	0.004	0.006	0.005	0.002	0.000	0.002	0.000	0.004
S	0.005	0.000	0.000	0.001	0.002	0.001	0.003	0.000	0.000	0.000	0.002	0.002	0.000	0.001	0.000	0.001	0.000	0.002	0.000	0.000	0.004
Si	0.010	0.006	0.004	0.006	0.011	0.017	0.009	0.019	0.013	0.015	0.013	0.045	0.040	0.022	0.013	0.015	0.034	0.014	0.002	0.034	0.037
P	2.957	2.965	2.942	2.868	2.895	2.958	2.945	2.945	2.946	2.902	2.961	2.957	2.927	2.928	2.951	2.916	2.973	3.003	2.917	2.939	2.921
Fe	0.004	0.003	0.001	0.017	0.002	0.000	0.000	0.000	0.000	0.010	0.003	0.000	0.000	0.002	0.008	0.007	0.004	0.016	0.005	0.010	0.002
Mn	0.003	0.000	0.000	0.004	0.006	0.000	0.000	0.001	0.000	0.000	0.009	0.002	0.002	0.000	0.005	0.000	0.001	0.000	0.010	0.000	0.003
Mg	0.002	0.001	0.010	0.000	0.002	0.000	0.000	0.000	0.004	0.000	0.002	0.005	0.000	0.000	0.001	0.000	0.005	0.000	0.000	0.000	0.000
Na	0.006	0.008	0.011	0.025	0.019	0.006	0.026	0.006	0.024	0.009	0.020	0.018	0.023	0.016	0.012	0.013	0.020	0.005	0.006	0.000	0.004
Ba	0.001	0.000	0.002	0.000	0.001	0.001	0.004	0.000	0.000	0.002	0.000	0.003	0.001	0.000	0.001	0.000	0.000	0.001	0.000	0.000	0.000
Sr	0.020	0.026	0.028	0.018	0.023	0.017	0.020	0.014	0.032	0.027	0.025	0.037	0.035	0.035	0.036	0.034	0.031	0.036	0.036	0.034	0.034
Ca	5.041	5.041	5.090	5.262	5.191	5.047	5.072	5.082	5.062	5.172	5.017	4.958	5.053	5.087	5.040	5.130	4.947	4.905	5.149	5.040	5.072
F site	0.746	0.706	0.758	0.715	0.893	0.709	0.750	0.742	0.861	0.928	0.875	0.893	0.747	0.716	0.809	0.761	0.705	0.764	0.716	0.762	0.631
P site	2.972	2.971	2.946	2.875	2.908	2.975	2.958	2.964	2.958	2.917	2.976	3.003	2.967	2.951	2.964	2.932	3.008	3.019	2.919	2.973	2.961
Ca site	5.077	5.079	5.142	5.328	5.243	5.072	5.121	5.103	5.122	5.220	5.076	5.022	5.114	5.140	5.103	5.183	5.008	4.962	5.207	5.084	5.115

Table 2 (continued)

	Pyroxenitic rocks												
	Apatite veins				Feldspathic pyroxenite		Fenite		Syenite			Trachyte	
Sample	GC 2701		GC 2705		GC 1524		GC 828		GC 832			GC 862	
Analysis spot	23–3	23–4	28–2	28–3	17–1	17–2	11–2	11–3	12–1	12–3	12–5	15–2	15–5
F[a]	2.02	2.16	2.31	2.28	3.41	3.06	3.44	3.29	3.17	3.45	3.03	3.68	3.62
Cl	–	–	–	0.03	–	–	–	0.06	–	–	–	–	–
SO_3	–	0.11	–	0.05	–	–	–	–	–	–	–	–	0.07
SiO_2	0.24	0.35	0.21	0.29	0.19	0.20	0.20	0.08	0.04	0.11	0.14	0.14	0.05
P_2O_5	40.34	41.13	41.23	40.82	39.72	39.31	40.12	40.90	39.27	41.16	40.89	40.31	40.11
FeO	–	–	0.05	–	–	0.20	–	0.08	–	0.09	0.07	–	–
MnO	–	0.09	–	–	–	0.07	–	–	0.09	0.12	–	0.13	–
MgO	–	–	–	–	–	–	–	–	–	–	–	–	–
Na_2O	0.15	–	–	0.13	0.06	–	–	–	0.22	0.14	0.20	–	0.09
BaO	0.18	0.07	–	–	0.12	–	–	–	–	–	0.01	–	–
SrO	0.56	0.62	0.69	0.64	1.25	1.18	0.09	0.10	4.21	3.60	3.47	0.22	0.35
CaO	54.59	53.95	54.83	54.71	54.29	54.31	54.53	55.26	51.86	52.18	51.83	54.79	55.79
O = F,Cl	0.85	0.91	0.98	0.96	1.44	1.28	1.45	1.39	1.33	1.45	1.28	1.55	1.52
Total	97.25	97.60	98.44	98.05	97.68	97.08	97.07	98.39	97.55	99.41	98.40	97.86	98.59
F	0.551	0.583	0.622	0.614	0.940	0.847	0.944	0.890	0.885	0.935	0.829	1.004	0.986
Cl	0.004	0.001	0.004	0.004	0.003	0.000	0.005	0.008	0.000	0.000	0.005	0.003	0.000
S	0.000	0.007	0.000	0.003	0.000	0.000	0.001	0.000	0.001	0.000	0.001	0.002	0.004
Si	0.021	0.029	0.018	0.024	0.016	0.017	0.017	0.006	0.004	0.010	0.012	0.012	0.004
P	2.947	2.975	2.970	2.954	2.929	2.915	2.950	2.963	2.936	2.990	2.992	2.948	2.923
Fe	0.000	0.001	0.003	0.003	0.002	0.014	0.003	0.005	0.000	0.006	0.005	0.003	0.000
Mn	0.000	0.007	0.000	0.002	0.000	0.005	0.000	0.000	0.007	0.009	0.000	0.009	0.002
Mg	0.000	0.003	0.002	0.000	0.003	0.000	0.006	0.003	0.000	0.002	0.000	0.000	0.000
Na	0.024	0.000	0.003	0.022	0.011	0.001	0.002	0.000	0.037	0.024	0.034	0.006	0.015
Ba	0.006	0.002	0.001	0.000	0.004	0.001	0.000	0.000	0.000	0.000	0.000	0.001	0.000
Sr	0.028	0.031	0.034	0.031	0.063	0.060	0.004	0.005	0.216	0.179	0.174	0.011	0.017
Ca	5.046	4.939	4.998	5.010	5.067	5.097	5.074	5.066	4.907	4.797	4.799	5.072	5.144
F site	0.555	0.585	0.625	0.618	0.943	0.847	0.949	0.899	0.885	0.935	0.833	1.007	0.986
P site	2.967	3.011	2.988	2.981	2.945	2.932	2.968	2.969	2.941	3.000	3.004	2.962	2.932
Ca site	5.105	4.983	5.041	5.068	5.150	5.178	5.089	5.079	5.167	5.017	5.013	5.102	5.178

The considered detection limit is 0.05 wt%; (-) in the table correspond to analyses below detection limit. The formulae are calculated to 12.5 O

[a]These measurements take into account an overestimation of ~ 0.35% due to third-order interference of P Kα on F Kα and potentially affected by grain orientation effect and anisotropic ion diffusion (Stormer et al. 1993; Goldoff et al. 2012)

Table 3 REE and Y (in ppm), ΣREE contents, La_N/Yb_N ratio and Eu*/Eu ratio of apatite from the Phalaborwa Complex (LA-ICPMS analyses). Normalization values: chondrites from McDonough and Sun (1995)

Sample	Analysis spot	Description–CL	La	Ce	Pr	Nd	Sm	Eu	Gd	Tb	Dy	Ho	Er	Tm	Yb	Lu	Y	ΣREE	La_N/Yb_N	Eu/Eu*
Phoscorite																				
GC 814	7B-1	Dark blue-green CL–grain (in cluster)	520	1435	175	819	161	34	115	11	47	5.9	10	0.87	3.8	0.39	142	3337	92	0.7
	7B-2	Dark blue-green CL-grain (in cluster)	584	1440	187	865	168	36	118	12	48	6.2	11	0.92	3.8	0.36	149	3478	104	0.7
	7B-6	Violet CL grain (in cluster)	603	1654	198	924	180	39	129	13	53	6.8	11	1.0	4.2	0.41	161	3818	97	0.7
GC 815	8–1	Dark CL overgrowth	462	1270	167	796	156	33	110	11	45	5.8	10	0.79	3.5	0.35	133	3070	89	0.7
	8–2	Dark CL–overgrowth	509	1452	181	847	163	35	115	11	47	6.0	10	0.92	3.7	0.33	141	3381	94	0.7
	8–5	Bright CL–early-formed apatite	989	2600	313	1427	271	56	188	18	78	9.7	17	1.5	6.3	0.62	231	5975	106	0.7
	8–8	Bright CL–early-formed apatite	843	2302	279	1288	246	52	172	17	72	8.9	15	1.3	5.5	0.53	213	5302	104	0.7
Carbonatite																				
GC 811	5–1	Dark blue CL–overgrowth	1417	3473	422	1944	328	39	177	15	56	6.7	11	0.92	3.4	0.34	166	7893	286	0.5
	5–2	Violet CL–early-formed apatite	2146	5280	650	2970	506	64	267	23	89	11	19	1.6	6.5	0.59	267	12,033	226	0.5
GC 814	7A-1	Bright CL–vicinity of a fissure	974	2854	349	1640	318	64	226	22	92	12	20	1.7	7.1	0.65	276	6580	94	0.7
	7A-2	Bright CL–vicinity of a fissure	934	2741	341	1600	316	63	223	21	88	11	19	1.6	6.1	0.57	263	6365	104	0.7
	7A-3	Dark CL core	573	1723	218	1019	205	43	145	14	62	7.8	13	1.1	4.8	0.50	189	4029	80	0.7
GC 1994	22A-1	Bright CL rim	1659	4348	526	2394	460	90	289	27	109	13	23	1.9	7.9	0.77	319	9947	144	0.7
	22A-3	Bright CL rim	1402	4069	503	2295	441	87	271	25	104	13	21	1.8	7.7	0.75	312	9241	123	0.7
	22A-4	Bright CL rim	1582	4877	635	3003	604	118	382	36	145	17	30	2.5	10	0.91	423	11,443	106	0.7
	22A-5	Dark CL core	676	2001	244	1198	234	48	155	14	59	7.2	12	1.0	4.5	0.40	169	4654	103	0.7
	22A-6	Dark CL core	761	2123	258	1210	232	46	152	14	57	6.7	11	1.0	4.0	0.38	165	4876	129	0.7
Pyroxenitic rocks																				
Massive pyroxenite																				
GC 1994	22C-1	Violet CL–early-formed apatite	1672	4180	496	2099	369	73	241	21	87	12	21	1.9	8.3	1.0	297	9283	136	0.7
	22C-2	Light violet CL–replacement/alteration	3695	8940	1102	4411	790	152	507	46	192	24	45	4.2	19	2.2	607	19,930	133	0.7

Table 3 (continued)

Sample	Analysis spot	Description–CL	La	Ce	Pr	Nd	Sm	Eu	Gd	Tb	Dy	Ho	Er	Tm	Yb	Lu	Y	ΣREE	La_N/Yb_N	Eu/Eu*
GC 2906	29–2	Violet CL grain	2310	5645	659	3050	590	109	381	34	137	17	31	2.9	14	1.5	437	12,981	112	0.7
	29–4	Dark blue CL grain/overgrowth	1183	2978	346	1597	303	56	195	17	68	8.9	16	1.4	6.8	0.75	222	6776	118	0.7
Micaceous pyroxenite																				
GC 2704	26A-1	Dark blue-greenish CL- overgrowth	655	1666	193	841	156	28	103	8.8	33	4.1	7.1	0.56	2.3	0.26	106	3698	191	0.6
	26A-2	Dark blue-greenish CL-overgrowth	683	1697	202	877	164	30	107	8.9	36	4.5	7.4	0.66	2.6	0.28	112	3820	181	0.6
	26A-3	Violet CL–early-formed apatite	1790	4163	493	2155	414	74	269	23	92	12	20	1.7	7.3	0.75	286	9515	166	0.6
	26A-4	Violet CL—core	2405	5501	629	2638	497	92	320	28	110	14	25	2.1	9.7	1.0	353	12,270	169	0.7
	26A-5	Dark blue-greenish CL—rim	1686	3824	437	1875	351	64	224	19	77	9.6	17	1.5	6.6	0.65	244	8594	174	0.7
	26A-6	Violet CL–core	1855	4252	488	2074	390	71	244	21	86	11	19	1.7	7.4	0.79	281	9521	171	0.7
	26A-7	Dark blue-greenish CL–rim	2007	4632	536	2304	434	78	272	25	96	12	22	1.9	8.6	0.86	312	10,429	159	0.6
GC 2707	30–2	Bright green CL–late infilling	1498	3463	386	1767	337	61	217	19	75	9.3	16	1.3	5.8	0.61	241	7858	176	0.6
	30–3	Violet CL–early-formed apatite	2849	6190	705	3041	572	105	357	32	130	16	28	2.5	11	1.1	414	14,041	176	0.7
Apatite veins																				
GC 2701	23–3	Dark blue CL core (in cluster)	1731	3948	451	2021	384	72	243	22	86	11	18	1.7	7.1	0.68	269	8996	166	0.7
	23–4	Violet CL–core (in cluster)	1743	4034	460	2067	385	71	247	22	87	11	19	1.6	7.2	0.76	273	9154	164	0.7
	23–5	Violet CL–core (in cluster)	1574	3716	424	1933	366	67	235	21	83	10	18	1.6	6.6	0.68	256	8456	162	0.7

Table 3 (continued)

Sample	Analysis spot	Description–CL	La	Ce	Pr	Nd	Sm	Eu	Gd	Tb	Dy	Ho	Er	Tm	Yb	Lu	Y	ΣREE	La_N/Yb_N	Eu/Eu*
GC 2705	28–1	Blue-greenish CL–rim (in cluster)	1354	3197	376	1574	300	54	191	16	65	8.1	14	1.2	5.4	0.54	211	7157	170	0.6
	28–2	Blue-greenish CL–rim (in cluster)	1495	3520	403	1710	318	57	201	18	69	8.7	15	1.3	5.8	0.61	225	7823	175	0.6
	28–3	Dark blue CL core (in cluster)	1718	4019	466	1952	367	66	236	20	79	10	18	1.5	6.6	0.67	263	8961	178	0.6
Feldspathic pyroxenite																				
GC 1524	17–1	Violet CL crystal	1730	3694	402	1734	316	58	218	20	82	12	25	2.6	12	0.98	351	8306	102	0.6
Fenite																				
GC 828	11–2	Bright green CL–rim/alteration	25	103	21	156	78	13	116	17	103	19	45	4.7	24	3.3	505	727	1	0.4
	11–3	Light blue CL–early-formed apatite	51	180	33	216	91	13	125	18	103	18	42	4.4	21	2.8	483	918	2	0.4
Syenite																				
GC 832	12–1	Intermediate blue-green CL–core	2772	5101	467	1792	296	54	209	22	113	20	50	6.1	31	3.3	980	10,937	60	0.6
	12–3	Bright violet CL–relict core?	2315	4844	476	1948	342	67	267	28	144	26	66	7.7	39	3.9	642	10,573	40	0.7
	12–5	Dark green CL–rim/replacement	2287	4510	442	1800	328	64	245	26	133	24	59	7.2	37	4.1	760	9966	42	0.7
Trachyte																				
GC 862	15–1	Bright blue CL zoning	752	1609	152	568	90	20	85	8.7	48	9.0	24	2.9	18	2.6	290	3389	29	0.7
	15–2	Bright blue CL zoning	848	1802	170	635	135	28	168	22	127	25	65	7.4	39	5.3	652	4078	15	0.6
	15–3	Greenish CL–rim	632	1251	135	569	211	33	308	48	308	62	172	22.6	134.7	18	1861	3903	3	0.4
	15–5	Reddish CL–core	569	1187	119	450	69	16	63	6.4	36	7.1	20	2.5	14.99	2.4	230	2562	26	0.7
Detection limit (d.l.)-ppm			0.143	0.285	0.041	0.159	0.059	0.020	0.069	0.006	0.020	0.005	0.012	0.005	0.020	0.006	0.05			

Table 4 Sr and O isotopic data of apatite from the Phalaborwa Complex (SIMS analyses)

Sample	Analysis spot	Description - CL	Sr (ppm)	$^{87}Rb/^{86}Sr$ (corr)	$^{87}Sr/^{86}Sr$ (corr)	1 σ	$^{87}Sr/^{86}Sr_{(i)}$(at 2060 Ma)	$\delta^{18}O_{(SMOW)}$(%)	1 σ
Phoscorite									
GC 814	7B-1	Dark blue-green CL–grain (in cluster)	4192	1.24E-05	0.7060	0.0005	0.7060	10.1	0.1
	7B-2	Dark blue-green CL–grain (in cluster)						10.3	0.1
	7B-3	Violet CL–grain (in cluster)	3594	1.476E-05	0.7072	0.0004	0.7072	9.2	0.2
	7B-4	Violet CL–grain (in cluster)						8.8	0.1
	7B-5	Violet CL–grain (in cluster)						9.7	0.1
	7B-6	Violet CL–grain (in cluster)	4013	1.623E-05	0.7067	0.0004	0.7067	8.5	0.1
GC 815	8-1	Dark CL–over-growth						8.0	0.1
	8-2	Dark CL–over-growth	3073	1.854E-05	0.7067	0.0004	0.7067	7.5	0.1
	8-3	Dark CL–over-growth						7.5	0.1
	8-4	Dark CL–over-growth	3030	1.986E-05	0.7070	0.0005	0.7070	7.4	0.1
	8-5	Bright CL–early-formed apatite	3463	1.675E-05	0.7063	0.0004	0.7063	7.2	0.1
	8-6	Bright CL–early-formed apatite						6.9	0.1
	8-7	Bright CL–early-formed apatite						7.2	0.1
	8-8	Bright CL–early-formed apatite	3405	1.763E-05	0.7078	0.0003	0.7078	7.0	0.2
Carbonatite									
GC 814	7A-1	Bright CL–vicinity of a fissure	3071	1.758E-05	0.7072	0.0003	0.7072	8.4	0.1
	7A-2	Bright CL–vicinity of a fissure	3094	1.776E-05	0.7068	0.0004	0.7068	7.5	0.1
	7A-3	Dark CL core	2634	2.148E-05	0.7070	0.0004	0.7070	8.5	0.2
GC 1994	22A-1	Bright CL rim	8454	2.284E-05	0.7052	0.0003	0.7052	9.2	0.1
	22A-2	Bright CL rim						9.4	0.1
	22A-3	Bright CL rim						7.3	0.1
	22A-4	Bright CL rim	10080	1.103E-05	0.7056	0.0004	0.7056	8.4	0.1
	22A-5	Dark CL core	7433	2.84E-05	0.7052	0.0004	0.7052	9.3	0.1
	22A-6	Dark CL core						9.5	0.1
Pyroxenitic rocks									
Massive pyroxenite									
GC 1994	22C-1	Violet CL–early-formed apatite	10675	2.982E-06	0.7056	0.0003	0.7056	7.9	0.2
	22C-2	Light violet CL–replacement/alteration	10425	7.644E-05	0.7058	0.0004	0.7058	7.4	0.2

Table 4 (continued)

Sample	Analysis spot	Description - CL	Sr (ppm)	$^{87}Rb/^{86}Sr$ (corr)	$^{87}Sr/^{86}Sr$ (corr)	1 σ	$^{87}Sr/^{86}Sr_{(i)}$(at 2060 Ma)	$\delta^{18}O_{(SMOW)}$(‰)	1 σ
GC 2706	29-1	Violet CL grain						8.3	0.1
	29-2	Violet CL grain	10745	1.915E-05	0.7134	0.0005	0.7134	8.1	0.1
	29-3	Violet CL grain						9.0	0.1
	29-4	Dark blue CL grain/overgrowth	11080	1.793E-05	0.7127	0.0003	0.7127	8.6	0.1
	29-5	Dark blue CL grain/overgrowth						8.3	0.2
Micaceous pyroxenite									
GC 2704	26A-1	Dark blue-greenish CL- overgrowth	9080	1.039E-05	0.7116	0.0003	0.7116	7.7	0.2
	26A-2	Dark blue-greenish CL- overgrowth	9309	7.669E-07	0.7108	0.0006	0.7108	8.0	0.2
	26A-3	Violet CL - early-formed apatite	9163	1.714E-07	0.7116	0.0004	0.7116	8.7	0.2
	26A-4	Violet CL–core	9258	7.757E-07	0.7108	0.0003	0.7108	7.1	0.2
	26A-5	Dark blue-greenish CL–rim	9249	5.095E-06	0.7110	0.0003	0.7110	8.2	0.2
	26A-6	Violet CL–core	10017	1.78E-06	0.7110	0.0003	0.7110	7.5	0.2
	26A-7	Dark blue-greenish CL–rim	9568	6.328E-06	0.7109	0.0004	0.7109	8.4	0.2
GC 2707	30-1	Bright green CL–rim	5641	9.247E-06	0.7104	0.0003	0.7104	8.7	0.1
	30-2	Bright green CL–late infilling	5416	8.909E-06	0.7110	0.0003	0.7110	9.1	0.1
	30-3	Violet CL–early-formed apatite	5794	8.77E-06	0.7103	0.0003	0.7103	8.0	0.1
	30-4	Violet CL–early-formed apatite						8.1	0.1
Apatite veins									
GC 2701	23-1	Violet CL–core (in cluster)	5277	1.013E-05	0.7112	0.0003	0.7112	8.1	0.1
	23-2	Violet CL–core (in cluster)						8.2	0.1
	23-3	Dark blue CL–core (in cluster)	5271	1.014E-05	0.7110	0.0004	0.7110	7.9	0.1
	23-4	Violet CL–core (in cluster)	5265	9.659E-06	0.7110	0.0003	0.7110	8.6	0.1
	23-5	Violet CL–core (in cluster)						7.8	0.1
	23-6	Violet CL–core (in cluster)						7.7	0.1

Table 4 (continued)

Sample	Analysis spot	Description - CL	Sr (ppm)	$^{87}Rb/^{86}Sr$ (corr)	$^{87}Sr/^{86}Sr$ (corr)	1 σ	$^{87}Sr/^{86}Sr_{(i)}$(at 2060 Ma)	$\delta^{18}O_{(SMOW)}$(‰)	1 σ
GC 2705	28-1	Blue-greenish CL–rim (in cluster)	9178	8.783E-05	0.7110	0.0003	0.7110	8.1	0.2
	28-2	Blue-greenish CL–rim (in cluster)	9171	9.568E-07	0.7106	0.0003	0.7106	7.6	0.2
	28-3	Dark blue CL- core (in cluster)	9287	1.113E-05	0.7117	0.0004	0.7117		
	28-4	Violet CL–core (in cluster)	9269	3.456E-05	0.7112	0.0003	0.7111		
	28-5	Violet CL–core (in cluster)	9157	3.075E-06	0.7108	0.0005	0.7108		
	28-6	Violet CL–core (in cluster)	9352	2.502E-06	0.7109	0.0004	0.7109		
Feldspathic pyroxenite									
GC 1524	17-1	Violet CL crystal	9639	4.399E-06	0.7092	0.0003	0.7092	8.6	0.1
	17-2	Violet CL crystal	9399	5.017E-06	0.7090	0.0002	0.7090		
Fenite									
GC 828	11-1	Light blue CL (mixed?) - core						8.0	0.1
	11-2	Bright green CL - rim/alteration	1102	0.0001399	0.7133	0.0006	0.7133	7.7	0.1
	11-3	Light blue CL–early-formed apatite	1094	0.000156	0.7124	0.0006	0.7124	7.9	0.1
Syenite									
GC 832	12-1	Intermediate blue-green CL–core	50054	1.52E-06	0.7084	0.0003	0.7084	5.1	0.1
	12-2	Intermediate blue-green CL–core						5.4	0.1
	12-3	Bright violet CL–relict core?	54061	1.69E-06	0.7079	0.0003	0.7079	5.4	0.1
	12-4	Bright violet CL–relict core?						5.2	0.1
	12-5	Dark green CL–rim/replacement	34618	1.973E-06	0.7095	0.0003	0.7095	4.4	0.1
	12-6	Dark green CL–rim/replacement						4.6	0.1
Trachyte									

Table 4 (continued)

Sample	Analysis spot	Description - CL	Sr (ppm)	$^{87}Rb/^{86}Sr$ (corr)	$^{87}Sr/^{86}Sr$ (corr)	1 σ	$^{87}Sr/^{86}Sr_{(i)}$(at 2060 Ma)	$\delta^{18}O_{(SMOW)}$(%)	1 σ
GC 862	15-1	Bright blue CL zoning	3817	9.588E-07	0.7170	0.0006	0.7170	1.6	0.2
	15-2	Bright blue CL zoning	2377	1.599E-06	0.7183	0.0009	0.7183	1.4	0.2
	15-3	Greenish CL–rim	2344	8.884E-07	0.7202	0.0004	0.7202		
	15-4	Dark blue CL zoning	5242	4.297E-06	0.7134	0.0004	0.7134		
	15-5	Reddish CL–core	6286	3.022E-07	0.7131	0.0004	0.7131	2.2	0.2

their potential loss in the course of the analysis. The data reported in Table 2 include a correction for excess F due to third-order interference of P Kα on F Kα was applied. Excess F was estimated at about 0.35% based on 15 measurements of F Kα in a phosphate that does not contain F (reference monazite at Univ. Würzburg). The measurements yielded a mean of 0.040% "fake" F per % P. A similar value (0.045%) was obtained by Potts and Tindle (1989). Note that grain orientation and anisotropic ion diffusion can also have a substantial influence on the measurement of F with the electron microprobe (e.g. Stormer et al. 1993; Goldoff et al. 2012).

Laser ablation-inductively coupled mass spectrometry (LA-ICPMS) was performed at GeoRessources (Nancy, France), with a GeoLas excimer laser (ArF, 193 nm, Microlas) coupled to a conventional transmitted and reflected light microscope (Olympus BX51) for sample observation and laser beam focusing and an Agilent 8900 triple quadrupole ICP-MS used in no-gas mode. The external standard was NIST SRM 610 and ^{44}Ca was used as internal standard. NIST SRM 614 and NIST SRM 612 silicate glasses were analyzed and considered as cross-calibration samples to control the quality of the analyses (precision, accuracy, repeatability) and to correct the possible drift during the analytical session (Jochum et al. 2011 for concentrations of the NIST silicate glasses). Ca contents in apatite were measured before LA-IC-MS analyses by EMPA (see above) to check the overall homogeneity of the apatite grains. Calcium concentration varies between the analyzed apatite grains (from 51.8 to 55.8 wt.% CaO; Table 2). Two different Ca concentrations, in weight percent, were used for internal standardization: 37.25 and 39.40 because of the variability of the Ca content encountered in apatite. The precisions were better than 10% for all REE. Data treatment was done using the software "Iolite" (Paton et al. 2011), following Longerich et al. (1996) for data reduction.

Oxygen (O) and Strontium (Sr) isotope compositions were obtained using a Cameca IMS 1280 HR2 ion microprobe (secondary ion mass spectrometry, SIMS) at CRPG Nancy. O isotopic ratios were measured with a Cs + primary ion beam of 3.5 nA focused on a 15 µm diameter area and with the electron gun used for the charge compensation. The negative secondary ions were measured with a mass resolution of 3000 (M/ΔM) with an energy slit of 35 eV. Before each measurement, the sample was pre-sputtered for 90 s with a beam rastering on 15 µm to clean up the sample surface, then the secondary beam was automatically centered in the field aperture and contrast aperture. The measurements were made on Faraday collectors in multicollection mode with a counting time of 150 s, with an internal precision of about 0.1 %. The instrumental mass fractionation was determined on the reference apatite Durango ($\delta^{18}O = 9.4$ %; Trotter et al. 2008), measured before and after each sample. Durango apatite is a fluorapatite with a composition overall similar to the measured samples (Marks et al. 2012). The external 1σ precision on the reference material ranges in between 0.15 and 0.20 %, with an instrumental isotopic fractionation on the $^{18}O/^{16}O$ ratio ranging in between 3 to 4 %. The reported errors are the quadratic sum of the internal error and of the reference material external error. The measured ratios are expressed in $\delta^{18}O$ values relative to the Standard Mean Ocean Water (SMOW) value.

The Sr isotope ratios were measured with the radio-frequency (RF) plasma source producing a O-primary beam accelerated at 13 kV and focused on the sample surface to produce a 10 µm spot with an intensity between 10 to 40 nA, depending on the Sr content of the samples. Positive secondary ions were extracted with a 10 kV potential. The positive secondary ions were measured at a mass resolution of 20 000 (M/ΔM), to remove almost all the isobaric interference on the Sr isotopes. Indeed, at this mass resolution, all the major Ca^{2+} overlapping masses are resolved, and Rb can be considered as a minor species. The measurements were

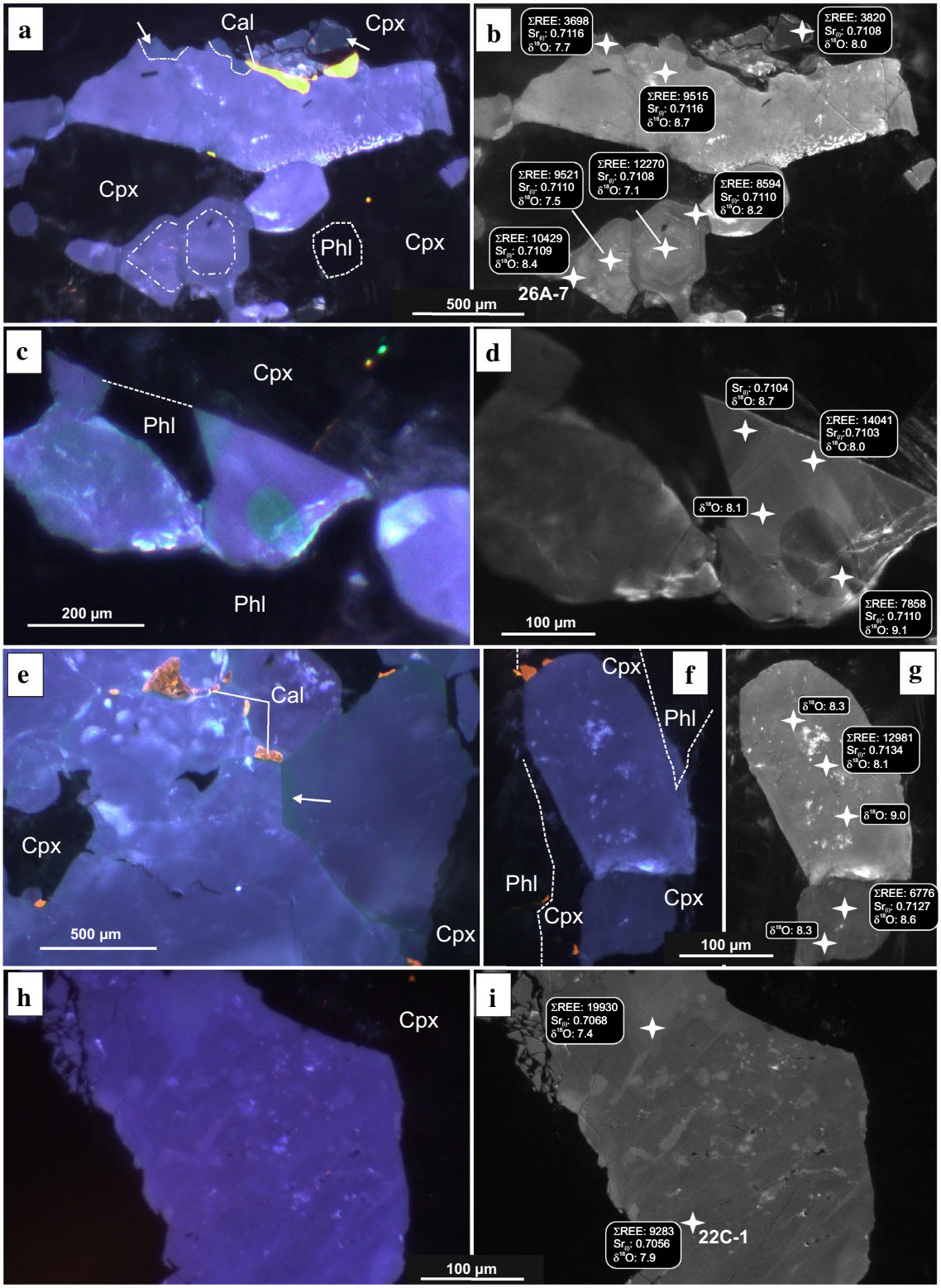

performed in mono-collection in ion counting mode, by peak switching over the masses 83.7 for the background measurement, ^{84}Sr, $^{84}Ca^{2+}$, ^{85}Rb, ^{86}Sr, ^{87}Sr and ^{88}Sr, with counting time of 3 s, 3 s, 3 s, 8 s, 16 s, 16 s and 8 s respectively. Each measurement consisted of 24 to 30 cycles (30–40 mn). The secondary ion intensity on ^{88}Sr was set in between 10^5 to 3×10^5 by adjusting the primary ion beam intensity. The instrumental mass fractionation between Sr isotopes was

◂**Fig. 3** Cathodoluminescence (CL) photomicrographs of the Phalaborwa pyroxenite rocks (and associated facies). Color CL in (**a**, **c**, **e**, **g** and **h**). Spectral CL (Nd^{3+} emission filtered at 880 nm) in (**b**, **d**, **f** and **i**); Cal–calcite, Cpx–clinopyroxene, Phl–phlogopite. The four-pointed stars represent the spots where EPMA, LA-ICPMS and SIMS analyses were performed. Related REE content (ΣREE in ppm), O isotope ratio (in %) and initial $^{87}Sr/^{86}Sr$ ratio (Sr(i)) are indicated in a black box. (a-b) Zoned apatite crystals with a blue-violet CL core and dark blue CL rim in a micaceous pyroxenite (sample GC 2704); The latest apatite overgrowth, which is observable on a seemingly corroded rim (arrows) is also characterized by a dark blue luminescence. The overgrowths exhibit weaker Nd-activation compared to the core, suggesting a lower concentration in LREE; (c-d) Green-luminescent apatite overgrowing early-formed violet-luminescent apatite and filling a corrosion gulf. Nd-activation is weaker in this overgrowth (micaceous pyroxenite, sample GC 2707); **e** closely-packed cluster of blue-violet-luminescing with a more greenish luminescence in the rim of some crystals (arrow) (apatite vein, sample GC 2702); **f**, **g** apatite grains in a massive pyroxenite with homogeneous blue-violet CL, likely a darker overgrowth on an early-formed brighter grain (sample GC 2706); **h**, **i** Violet-luminescent apatite crystal exhibiting a heterogeneous texture which is better resolved in the spectral image. The apatite was partly altered/corroded and overgrown by apatite with a higher Nd-activation (massive pyroxenite, sample GC 1994)

corrected for a $^{86}Sr/^{88}Sr$ ratio of 0.1194. The ^{87}Rb isobaric interference on ^{87}Sr was corrected for the measured ^{85}Rb count rate, a $^{87}Rb/^{85}Rb$ ratio of 0.3825, and the instrumental mass fractionation measured for Sr. The reported errors include the errors on the measured $^{87}Sr/^{86}Sr$, $^{86}Sr/^{88}Sr$ and $^{85}Rb/^{86}Sr$ ratios. The errors range from 0.3 to 2 % (1σ), depending on the Sr and Rb contents. The Sr contents were calculated using the measured $^{86}Sr/^{84}Ca_2$ ratio and the Durango apatite ($^{87}Sr/^{86}Sr = 0.7063$; Yang et al. 2014) as a reference material.

Results

Petrologic description

Apatite in pyroxenitic rocks, phoscorite and carbonatite

In most of the rocks constituting the Phalaborwa Complex, apatite is present either as isolated euhedral to anhedral crystals stubby or elongated (from a few tens of micrometers up to a few millimeters in size) or clusters of crystals, which can in some instances, as in phoscorite and apatite veins, form massive pure apatite veins.

In the pyroxenitic rocks, apatite is mostly associated with clinopyroxene (diopside) and phlogopite in variable proportions, with K-feldspar and calcite as interstitial minerals and sporadic occurrences of amphibole and magnetite. Feldspathic pyroxenite is characterized by an assemblage dominated by K-feldspar, clinopyroxene and, more rarely, phlogopite and amphibole. Apatite crystals in the pyroxenitic rocks exhibit a rather uniform blue-violet CL. However, some faint but distinctive textures are observed, including a rounded zonation (Fig. 3a, b) and embayments (Fig. 3c, d). Blue/violet CL is well known from fluorapatite in carbonatites and is usually assigned to emission centers caused by substituting REE (e.g. Marshall 1988; Blanc et al. 2000; Kempe and Götze 2002; Baele et al. 2019). The predominant blue CL of such apatite is caused by Eu^{2+} activation but violet to reddish/brownish shades can develop due to the superimposition of Sm^{3+} activation and greenish shades due to Dy^{3+} and/or Mn^{2+} activation. Green CL is usually observed in apatite rims with either a gradational or sharp boundary (Fig. 3c, e). In the latter case, the green CL highlights secondary apatite in late overgrowths, which can occur within embayments, giving the false impression of early-formed cores in section (Fig. 3c). Spectroscopic data show that the green luminescence in our apatite samples is mostly caused by Dy^{3+} activation (see Supplementary Material).

The CL texture is better defined under spectral CL imaging (Fig. 3b, d, g, i). Overall, the deep-violet and green-luminescent outer rims of zoned crystals (Fig. 3a, e) and the dark blue and green-luminescent overgrowths (Fig. 3a, c, f) of apatite show a weaker activation by Nd^{3+} compared to the blue-violet luminescent primary apatite. However, in one case (sample GC 1994; Fig. 3h, i), secondary apatite has a stronger Nd^{3+} activation. In this particular case, the texture is more complex and could be due to alteration along cleavage plans.

Phoscorites are rocks that are mostly made up of olivine (variably serpentinized), calcite (with associated dolomite grains), magnetite, phlogopite, and locally clinopyroxene. Some of the characteristics of apatite CL in pyroxenitic rocks mentioned above are also observed in phoscorite. Early-formed apatite has a violet-blue CL with some more greenish zones, especially but not systematically in the outer rim and overgrowth of the crystals. The green CL is also accompanied by a decrease in Nd-activation from early-formed to late-formed apatite (Fig. 4a, b).

In the carbonatites, apatite is commonly present as scattered, locally needle-shaped, crystals exhibiting a violet-blue luminescence. It is embedded within calcite with either a dull brownish or a bright yellow-orange luminescence (Fig. 4c), which is attributed to variable concentration in trace Mn^{2+} (CL activator) and Fe^{2+} (CL inhibitor) substituting for Ca^{2+} in calcite (e.g. Habermann et al. 2000). The CL of apatite is in many cases difficult to observe as it can be overwhelmed by the intense yellow-orange CL of calcite. Our observations suggest that the dull-CL calcite formed earlier than the bright-CL calcite (Fig. 4c). The orange-luminescent calcite frequently contains exsolution lamellae of red-luminescent dolomite. However, both calcite types are characterized by low Mg contents, between 2 and 3 wt% (average of SEM–EDX analyses), which is consistent with

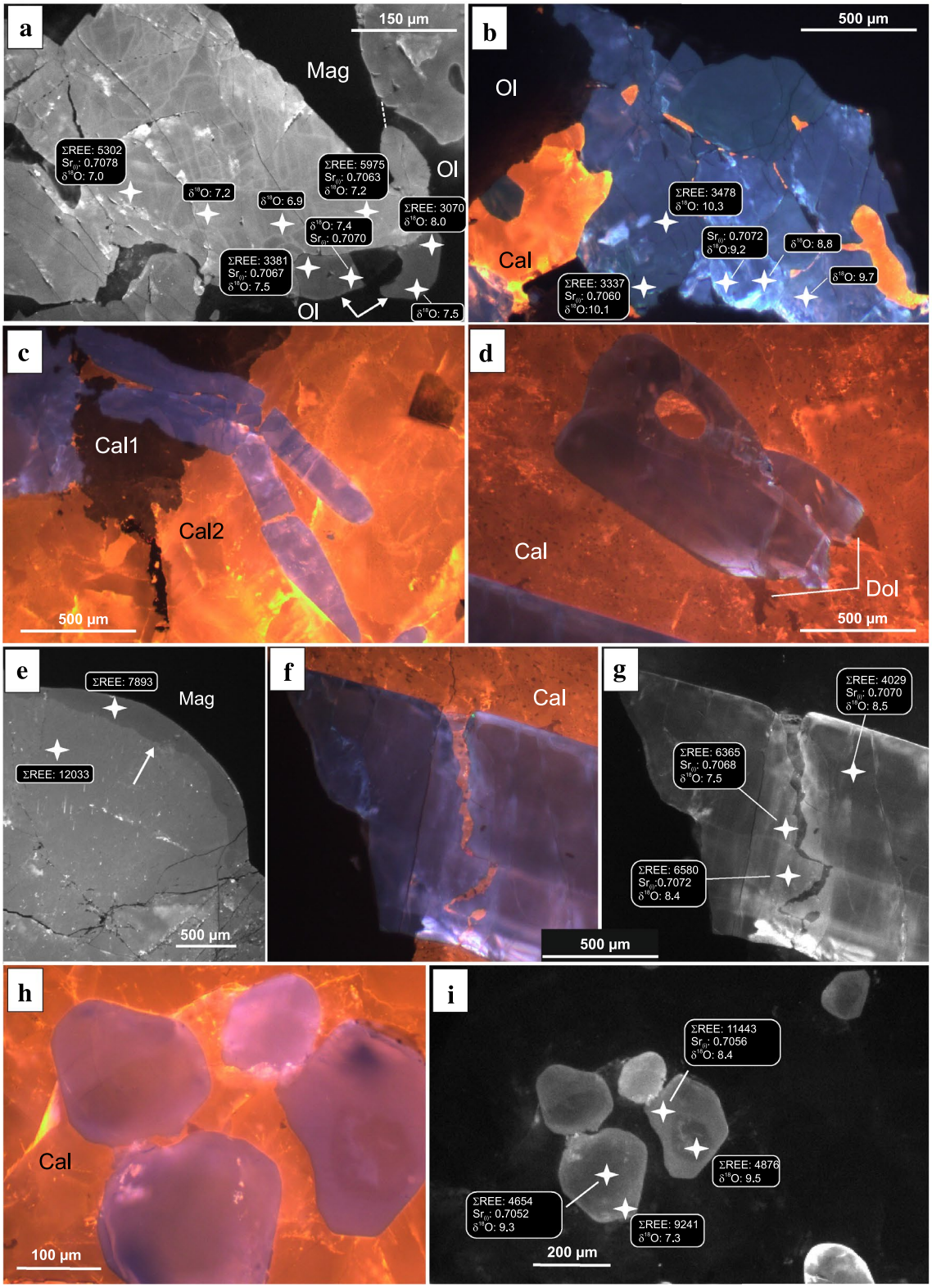

the "banded carbonatite" type (Eriksson 1989). Many of the carbonatite-hosted apatite crystals display evidence of corrosion/resorption (Fig. 4d, e, h), brecciation (Fig. 4c) and/or fissures (Fig. 4f,g). Again, apatite overgrowths show a decrease in Nd-activation compared to primary apatite as illustrated in a pluri-millimetric crystal embedded in magnetite (Fig. 4e). By contrast, a stronger Nd-activation is observed within the walls of fissures affecting apatite

◂**Fig. 4** Cathodoluminescence (CL) photomicrographs of Phalaborwa phoscorite and carbonatite; Color CL in (**b**–**d**, **f** and **h**); Spectral CL (Nd^{3+} emission filtered at 880 nm) in (**a**, **e**, **g** and **i**); Cal–calcite, Dol–dolomite, Mag–magnetite, Ol–olivine. The four-pointed stars represent the spots where EPMA, LA-ICPMS and SIMS analyses were performed. Related REE content (ΣREE in ppm), O isotope ratio (in %) and initial $^{87}Sr/^{86}Sr$ ratio (Sr(i)) are indicated in a black box. **a** Closely-packed cluster of apatite crystals in phoscorite. Apatite overgrowths (indicated by arrows) are characterized by a decrease in Nd-activation (sample GC 815); **b** blue-violet-luminescing apatite crystals in phoscorite (sample GC 814) with some zones showing a more greenish CL (in the lower-left and upper of the cluster); **c** needle-shaped apatite crystals extending across the boundary between dull- and bright-luminescing calcite (Cal 1 and Cal 2, respectively); The deformation pattern of the apatite crystals suggests they were set in Cal 1 and broke before the crystallization of Cal 2 (banded carbonatite, sample GC 809); **d** apatite showing corrosion/resorption texture. Note the presence of dolomite in the calcitic matrix (banded carbonatite, sample GC 814); **e** magnetite-hosted apatite crystal with corrosion (arrow) prior to overgrowth; Apatite overgrowth has weaker Nd-activation than primary apatite (banded carbonatite, sample GC 811); **f**, **g** fissured violet-luminescing apatite crystal in carbonatite with increased Nd-activation in fissure walls (banded carbonatite, sample GC 814); **h**, **i** Cluster of zoned apatite crystals in carbonatite, with stronger Nd-activation in their outer rim GC 1994)

crystals in carbonatite (Fig. 4f, g) and within the outer rim of zoned apatite crystals hosted in similar carbonatite rock (Fig. 4h, i).

Apatite in fenite, syenite and trachyte

Apatite is present in fenite as small stubby anhedral crystals set in a rock predominantly made up of quartz, blue-luminescent K-feldspar, and red-luminescent albite (Fig. 5a). The red emission, due to Fe^{3+}-activation, is commonly observed in feldspars from fenitized rocks (Marshall 1988; Mariano and Mariano 2012). Apatite is green-luminescent due to Dy-activation (Fig. 5a and spectra in the Supplementary Material), with some veining/alteration revealed by CL spectral imaging (Fig. 5b). A thin discontinuous apatite overgrowth with stronger Nd-activation is locally overlain by dark-luminescing apatite associated with fluorbritholite (Fig. 5c).

Syenite comprises red-luminescent K-feldspar and albite (Fig. 5d) and non-luminescent aegirine, amphibole, quartz and phyllosilicate (Fig. 5e). Apatite appears as stubby crystals with a corroded rim and a complex texture under CL. Apatite luminescence is mostly blue-violet with irregular dark blue and green-luminescent zones, the latter tending to concentrate along the outer rim (Fig. 5d).

Trachyte is mostly made up of red-luminescent albite (related to Fe^{3+}-activation; Götte 2009), mica (that enhances the fluidal texture of the rock), K-feldspar, quartz and aegirine. Apatite in trachyte commonly occurs as elongated crystals showing a zoned and veined pattern under CL (Fig. 5f). A reddish-brown luminescent core is surrounded by blue-luminescent apatite with an overall increase in Nd-activation. A green CL rim is locally observed with an associated decrease in Nd-activation (Fig. 5g).

Mineral chemistry

Apatite from Phalaborwa shows a moderate range of P_2O_5 concentration (38.12–41.44 wt.%) and a rather large range of CaO content (51.83–55.79 wt.%, see Table 2), which indicates significant substitution at Ca and P sites (simple or coupled substitutions with F, Si, Sr and REE, for instance; Pan and Fleet 2002).

Fluorine contents vary between 2.02 and 3.41 wt.% for apatite from carbonatite, phoscorite and pyroxenitic rocks, and between 3.03 to 3.68 wt.% for apatite in fenite, syenite and trachyte. All F contents are below the theoretical maximum in apatite (3.73%). Apatite in all rock types has low Cl contents (≤ 0.09 wt.%). SrO contents range from 0.09 to 0.73 wt.% in most of the apatite grains analyzed but are higher in apatite from feldspathic pyroxenite (~ 1.21 wt.%) and syenite (3.47–4.21 wt.%). SiO_2 contents are low to moderate in most grains analyzed, varying from below the detection limit to 0.22 wt.% but are somewhat higher in apatite hosted by pyroxenitic rocks (up to 0.52 wt.% SiO_2). Low to moderate contents are also observed for FeO (up to 0.24 wt.%) and Na_2O (≤ 0.22 wt.%). SO_3 content is low (≤ 0.11 wt.%), as are BaO and MnO contents that do not exceed 0.18 wt.% and 0.13 wt.%, respectively. MgO content is above the detection limit (0.08 wt.% MgO) in only one sample.

Most of the analyzed apatite grains have similar REE patterns (Table 3), except those hosted by fenite and trachyte (Fig. 6a–i). Apatite from phoscorite has high total REE contents (3070—5975 ppm), with a strong enrichment in LREE (La_N/Yb_N = 89–106) and a moderate negative Eu anomaly (0.7; Fig. 6a). Apatite from carbonatite has more variable REE and LREE enrichment (ΣREE = 3691–12,033 ppm; La_N/Yb_N = 63–286), with a similar Eu anomaly (Eu/Eu* = 0.5–0.7) (Fig. 6b,c; Table 3). Similar trends are observed for apatite from pyroxenite, which is, however, overall richer in REE (ΣREE = 3698–19,930 ppm), with strong LREE enrichment (La_N/Yb_N = 112–191) and still moderate negative Eu anomaly (Eu/Eu* = 0.6–0.7) (Fig. 6d–g).

Apatite in the syenite displays REE patterns that are similar in shape to those in apatite from pyroxenite, phoscorite and carbonatite (Fig. 6h). It is REE-enriched (ΣREE = 9966–10,937 ppm), and corresponding patterns display LREE enrichment (La_N/Yb_N = 40–60), and negative Eu anomalies of about 0.7. Apatite in the fenite is characterized by MREE-enriched patterns (Fig. 6h; ΣREE = 727 and 918 ppm; La_N/Yb_N = 0.7 and 1.6) and a slightly more pronounced negative Eu anomaly (Eu/Eu* = 0.4). Apatite in trachyte is REE-rich (ΣREE = 2562–4078 ppm), and REE patterns show a marked (but variable) enrichment in MREE

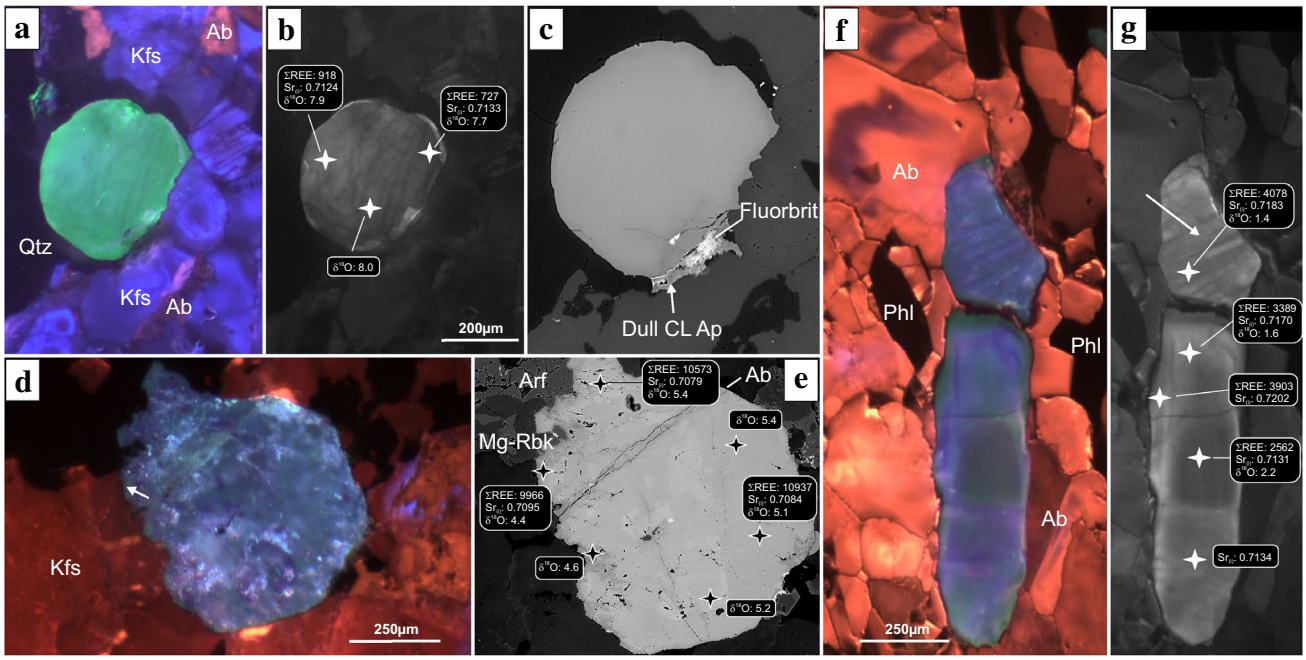

Fig. 5 Cathodoluminescence (**a**, **b**, **d**, **f**, **g**) and backscattered electron (**c**, **e**) micrographs of fenite, syenite and trachyte from Phalaborwa. Color CL in (**a**, **d**) and (**f**). Spectral CL (Nd^{3+} emission filtered at 880 nm) in (**b**) and (**g**); Ab–albite, Arf–arfvedsonite, Fluorbrit–fluorbritholite, Kfs–K-feldspar, Mg-Rbk–Mg-riebeckite, Qtz–quartz, Phl-phlogopite. The four-pointed stars represent the spots where EPMA, LA-ICPMS and SIMS analyses were performed. Related REE content (ΣREE in ppm), O isotope ratio (in ‰) and initial $^{87}Sr/^{86}Sr$ ratio (Sr(i)) are indicated in a black box. **a–c** Apatite crystal in fenite comprising quartz, blue-luminescing K-feldspar and pink-luminescing albite; Apatite is green-luminescent with some vein texture visible in the spectral image. A thin discontinuous overgrowth with strong Nd-activation, which is locally overlain by non-luminescent apatite associated with fluorbritholite (sample GC 828); **d–e** stubby crystal of apatite in syenite formed by red-luminescent K-feldspar and albite, and non-luminescent amphiboles (Mg-riebeckite and arfvedsonite). Apatite exhibits a complex luminescence texture. The primary blue-violet-luminescent apatite is partly replaced by dark blue and green-luminescent apatite along cracks and rim, as indicated by the arrow (sample GC 832). This texture is visible in backscattered electron image (**e**). **f**, **g** Zoning and veining texture in an elongated apatite crystal in trachyte made of red-luminescent albite and non-luminescent phlogopite. Apatite luminescence is predominantly reddish-brown in the core and blue in the outer part, with a discontinuous green-luminescent rim. Overall, a gradual increase in Nd-activation is observed, except in the outermost, discontinuous green-luminescent apatite (trachyte, sample GC 862). The arrow highlights alteration patterns

and HREE (La_N/Yb_N ranges from 3.2 to 29. Figure 6i), with comparable negative Eu anomalies ($Eu/Eu^* = 0.4–0.7$).

Consistently with our observations of the Nd^{3+} emission under spectral CL, geochemical intra-grain variability is locally important in apatite, with an overall correlation between higher REE concentration and CL intensity. A close examination of the REE patterns (and intra-grain variability) of apatite from phoscorite (Fig. 6a) shows that bright violet-luminescent apatite is enriched in REE compared to dark blue/green-luminescent apatite. Dark blue-luminescent overgrowths are consistently depleted in REE compared to early-formed apatite. In carbonatite-hosted apatite, the bright-luminescent rims and alteration zones (adjacent to fissures) are enriched in REE compared to the core and unaltered zones (Fig. 6b). In the same way, the dark blue-luminescent apatite overgrowths in carbonatite are depleted in REE compared to the early-formed violet-luminescent apatite (Fig. 6c). In pyroxenitic rocks, the dark blue or green-luminescent apatite overgrowths and rims are depleted in REE compared to corresponding early-formed apatite (crystal cores in the case of zoned apatite) (Fig. 6d–g). However, in one massive pyroxenite (sample GC 1994), the bright violet-luminescent apatite replacing a dark violet-luminescing apatite exhibits REE enrichment (Fig. 6d). Apatite in syenite, regardless of its luminescence (which is variable in a single grain, see Fig. 5d), has uniform REE patterns (Fig. 6h). By contrast, REE patterns of fenite-hosted apatite differ considerably as they are MREE enriched and exhibit a pronounced Eu anomaly. The bright green-luminescent rim/alteration zone is depleted in REE compared to the early-formed light blue-luminescing apatite (Fig. 6h). REE patterns in zoned apatite grains from trachyte are also significantly different from those in apatite in the other rock types of the Phalaborwa Complex, which are comparatively enriched in MREE and HREE. The concentration of these elements increases from the core to the rim (Fig. 6i), which corresponds to CL observations under spectral imaging in the near infrared range (Fig. 5g).

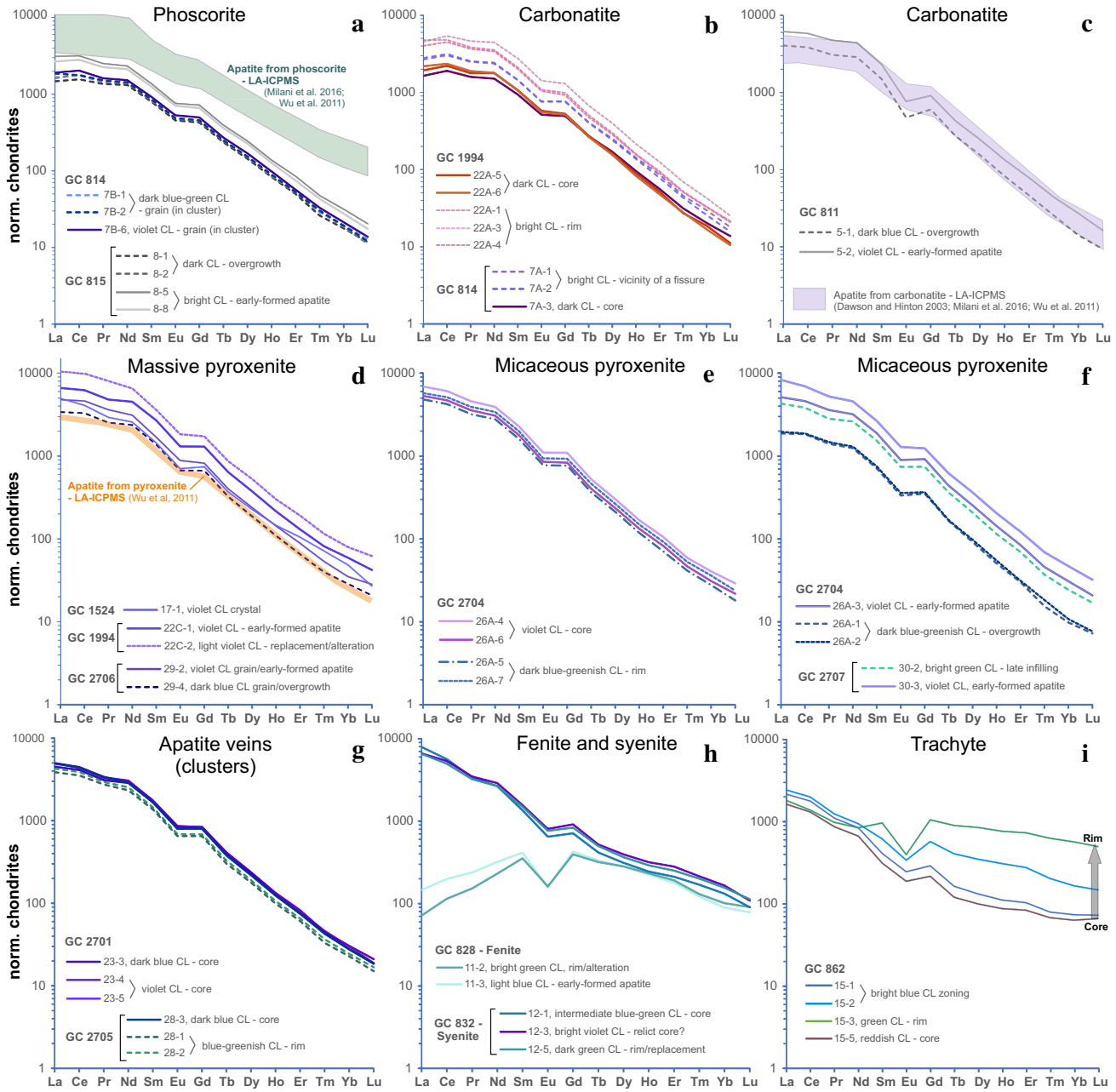

Fig. 6 REE patterns of apatite in the different rock types of the Phalaborwa Complex; **a** phoscorite, (**b**, **c**) carbonatite, (**d**) massive pyroxenite, (**e**, **f**) micaceous pyroxenite, (**g**) apatite veins, (**h**) fenite and syenite, (**i**) trachyte; REE patterns are normalized to chondrite values from McDonough and Sun (1995)

Oxygen and strontium isotope ratios

The O isotopic compositions of the Phalaborwa apatites are given in Table 4 and shown in Fig. 7. The $\delta^{18}O$ values vary from 6.9 to 10.3 ‰ for apatite from phoscorite and between 7.3 and 9.5 ‰ for apatite from carbonatite. Most of the $\delta^{18}O$ values of apatite from pyroxenitic rocks fall within the same range (7.1 – 9.1 ‰). Intra-grain variation in apatite from these rock types is typically about 1 ‰, irrespective of the variation in terms of luminescence or trace element contents. Larger variations were, however, noted in two cases: (1) in two apatite generations coexisting in a single grain, with $\delta^{18}O$ values varying from 8.0 ‰ in early-formed violet-luminescent apatite to 9.1 ‰ in bright green-luminescent overgrowth (micaceous pyroxenite, sample GC2707; Fig. 3c,d)), and (2) in a crystal cluster hosted by a phoscorite (sample GC814), where the $\delta^{18}O$ ratios seemingly vary according to the luminescence of apatite (from 8.5 ‰ in the early-formed

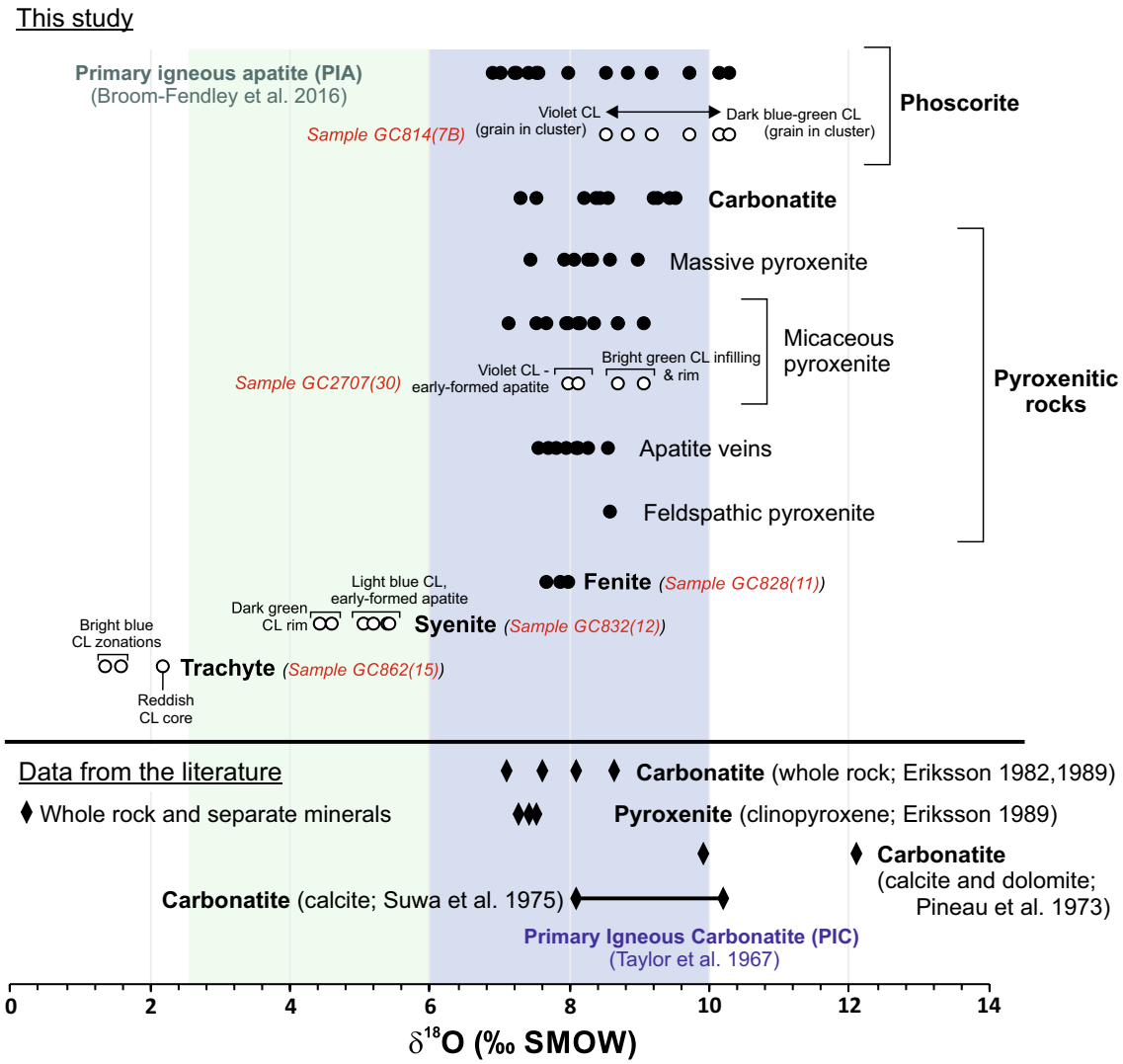

Fig. 7 In-situ $\delta^{18}O$ for apatite hosted in the different rock types of the Phalaborwa Complex; data from the literature are given for comparison

violet-luminescent apatite to 10.3 % in late dark blue-green-luminescent apatite). The $\delta^{18}O$ values of apatite in the fenite are consistent with those in rocks mentioned here above (7.7–8.0 %). By contrast, in syenite and trachyte, the O isotope composition of apatite is significantly lighter (4.4–5.4 % and 1.4–2.2 %, respectively), with intra-grain variations of about 1.5–2 %.

The Sr isotopic compositions of the Phalaborwa apatites are presented in Table 4 and Fig. 8. The initial isotopic ratios have been calculated based on an emplacement age at 2060 Ma (in-situ U–Pb ages on zircon and baddeleyite; Wu et al. 2011). The initial $^{87}Sr/^{86}Sr$ ratios ($Sr_{(i)}$) vary considerably. Apatite from carbonatite is characterized by the least radiogenic initial $^{87}Sr/^{86}Sr$ ratios, ranging from 0.7052 to 0.7072. One apatite from the massive pyroxenite yielded initial ratios in the same compositional range ($Sr_{(i)}$: 0.7056 and 0.7058). Apatite in phoscorite differs from apatite in carbonatite, with $^{87}Sr/^{86}Sr_{(i)}$ between 0.7060 and 0.7078. Apatite from micaceous pyroxenite and apatite veins form another group with $Sr_{(i)}$ ratios consistently between 0.7103 and 0.7117. The initial $^{87}Sr/^{86}Sr$ ratios of apatite from syenite (0.7079–0.7095) are slightly higher than the apatite in carbonatite and phoscorite, as are the $Sr_{(i)}$ values of apatite in syenite (0.7090 and 0.7092). The Sr isotopic composition of apatite in the fenite is even more radiogenic (0.7124–0.7133) than the apatite from massive pyroxenite (sample GC 2706; $Sr_{(i)} = 0.7127$ and 0.7134). Apatite in the trachyte has the most radiogenic Sr isotopic compositions and the largest intra-grain variability, with $^{87}Sr/^{86}Sr_{(i)}$ ranging from 0.7131 to 0.7202.

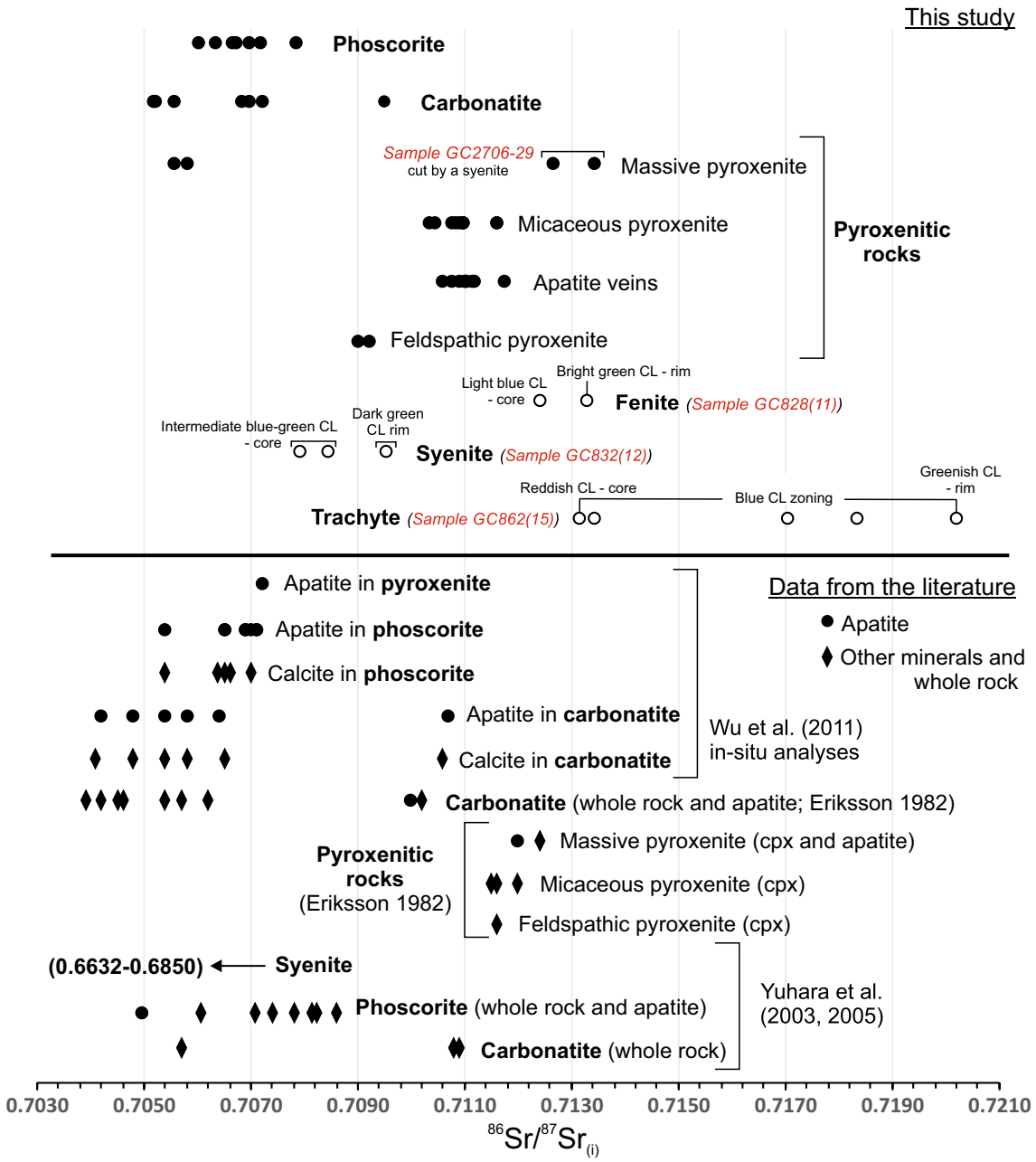

Fig. 8 In-situ $^{87}Sr/^{86}Sr_{(i)}$ for apatite hosted in the different rock types of the Phalaborwa Complex; data from the literature are given for comparison

Discussion

New insights into magmatic processes and sources at Phalaborwa

Oxygen and Sr isotope data provide useful insights into the genetic processes behind the different generations of apatite in the various host rocks at Phalaborwa. The low $^{87}Sr/^{86}Sr_{(i)}$ of 0.7052–0.7078 obtained on apatite from carbonatite and phoscorite indicate that the parental mantle-derived magmas from which these apatites crystallized were hardly contaminated by continental crust, in agreement with previous studies by Wu et al. (2011; apatite and calcite in-situ analyses), Eriksson (1982, 1989; separate minerals and whole rock analyses), and Yuhara et al. (2003, 2005; apatite and whole rock analyses) (Fig. 8). They also overlap in $\delta^{18}O$ (Fig. 9a), suggesting a common magmatic origin. The slight isotopic heterogeneity in apatite from phoscorite and carbonatite is probably due to some magma mixing under open-system conditions (Milani et al. 2017). Most of $\delta^{18}O$ values plot in

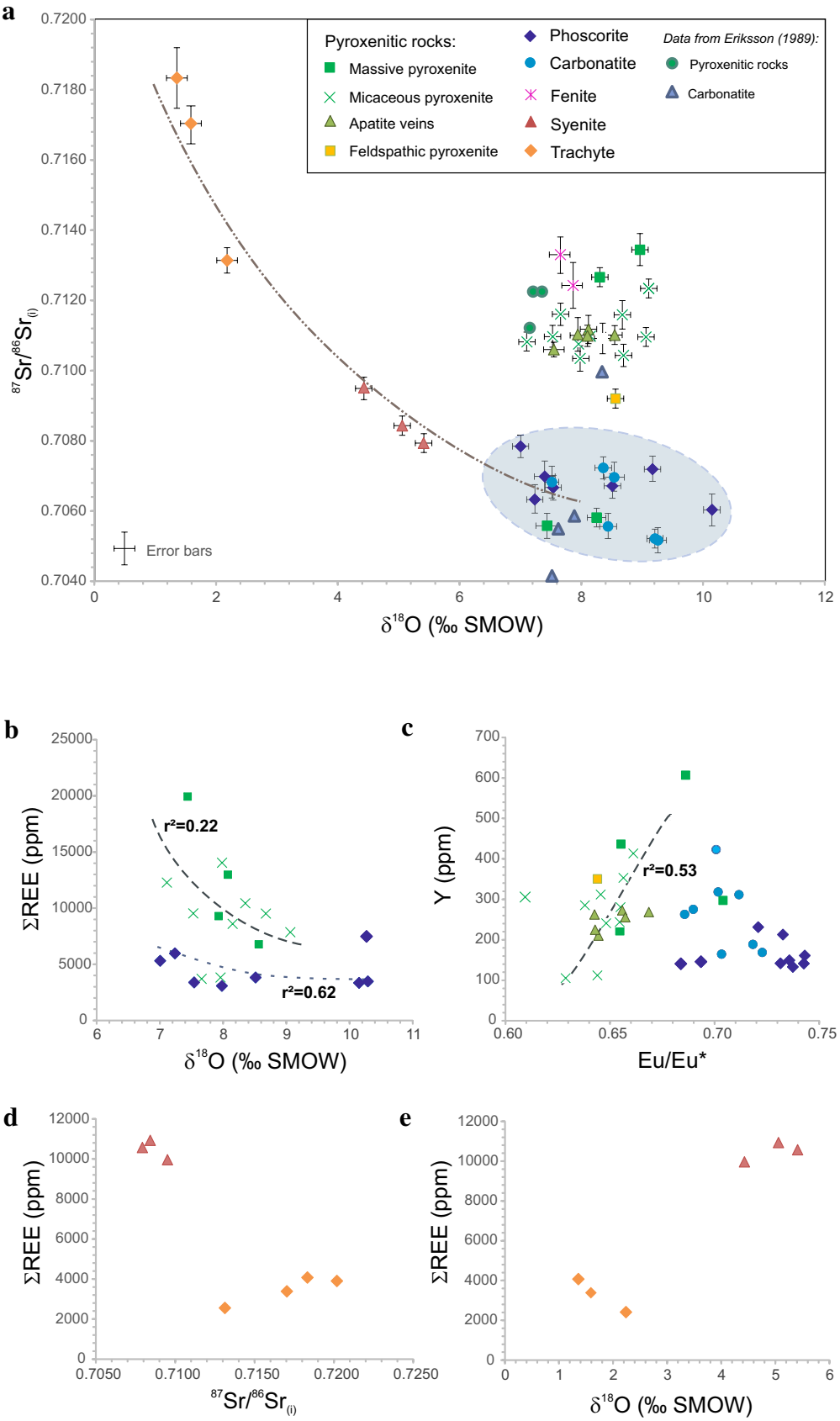
a
Pyroxenitic rocks:
Massive pyroxenite
Micaceous pyroxenite
Apatite veins
Feldspathic pyroxenite
Phoscorite
Carbonatite
Fenite
Syenite
Trachyte
Data from Eriksson (1989):
Pyroxenitic rocks
Carbonatite
Error bars
87Sr/86Sr(i)
δ18O (‰ SMOW)
b
r²=0.22
r²=0.62
ΣREE (ppm)
δ18O (‰ SMOW)
c
r²=0.53
Y (ppm)
Eu/Eu*
d
ΣREE (ppm)
87Sr/86Sr(i)
e
ΣREE (ppm)
δ18O (‰ SMOW)

◂**Fig. 9** Correlation between **a** $^{87}Sr/^{86}Sr_{(i)}$ and $\delta^{18}O$ for apatite hosted in the different rock types of the Phalaborwa Complex. Phoscorite and carbonatite define the light blue field; **b** ΣREE and $\delta^{18}O$ for apatite from phoscorite, massive pyroxenite and micaceous pyroxenite (LA-ICPMS and SIMS analyses); **c** Y content and Eu anomaly for apatite from phoscorite, carbonatite and pyroxenitic rocks; **d** ΣREE and $^{87}Sr/^{86}Sr_{(i)}$ and **e** ΣREE and $\delta^{18}O$ for apatite from syenite and trachyte (LA-ICPMS and SIMS analyses)

the field defined for primary igneous carbonatite by Taylor et al. (1967). They are, however, outside of the field (Fig. 7) for primary igneous apatite defined by Broom-Fendley et al. (2016a). Our data are consistent with the $\delta^{18}O$ values previously obtained by Pineau et al. (1973), Suwa et al. (1975) and Eriksson (1982) on carbonatite (whole rock analyses) and calcite (as separate minerals). The meaning of this apparent consistency ($\delta^{18}O$ comprised in a narrow range from about 7 to 10 per mil) remains uncertain. Apatite is largely considered as resistant to re-equilibration and isotopic resetting at low temperature (e.g. Cole and Chakraborty 2001), unlike calcite (e.g. Pineau et al. 1973). This implies that $\delta^{18}O$ of apatite and calcite don't necessarily result from the same processes, thus complicating the discussion of these data. If we consider nonetheless that the processes recorded by these minerals are similar (only magmatic with little or no effect of low-temperature fluids), then a higher fractionation could be expected between apatite and calcite (Fortier and Lüttge 1995). The relative consistency of the $\delta^{18}O$ can be explained either if apatite and calcite were in equilibrium at high crystallization temperature (Fortier and Lüttge 1995) or if these minerals crystallized in equilibrium with a melt that experienced a slight change of composition between the times apatite and calcite, respectively, formed.

Regarding the pyroxenitic rocks, our data are overall consistent with those published by Eriksson (1982, 1989) (Figs. 7, 8, 9a), though a shift in $\delta^{18}O$ is observed between clinopyroxene and apatite. Apatite in the various pyroxenitic rocks is, with two exceptions, significantly enriched in ^{87}Sr compared with phoscorite and carbonatite, but has similar $\delta^{18}O$ ratios (Fig. 9a). This enrichment could be related to crustal contamination and/or metasomatism at different stages of magma evolution. However, the very high Sr content of apatite in pyroxenitic rocks (~ 10,000 ppm, Table 4) makes it less susceptible to enrichment in radiogenic Sr due to such processes. Instead, the more radiogenic values would highlight a (slightly) different metasomatised mantle source for pyroxenitic rocks. The high Sr contents of the minerals forming these rocks (> 500 ppm Sr in clinopyroxene; Eriksson 1982) argue for a parent liquid enriched in Sr. The higher initial $^{87}Sr/^{86}Sr$ ratios of the source would be achieved through a long enough residence time and a high Rb content of the source of the liquid (which is likely considering the high Rb content of phlogopite of above 600 ppm; Ericksson 1989). Exceptions are two analyses from massive pyroxenite, crosscut by banded carbonatite (sample GC 1994). They plot within the Sr and O isotopic fields defined for apatite from phoscorite and carbonatite (Fig. 9a). This may be explained by carbonatite-related apatite crystallization in the massive pyroxenite, in which case it would not be representative of the environment of pyroxenite formation.

The alkaline character of fenite is highlighted by the partial replacement of the primary minerals constituting the country rock by red-luminescent feldspar (albite in Fig. 5a). Its highly radiogenic composition can be explained by interaction, to some extent, with the surrounding Archean continental crustal rocks. Both syenite and trachyte (respectively from Kgopoeloe and Spitskop) are clearly related to alkaline magmatism. This is supported by: (1) the red, Fe^{3+}-activated luminescence of the feldspar forming these rocks (K-feldspar in syenite and albite in trachyte, Fig. 5d, f) (Marshall 1988), and (2) the characteristic LREE enrichment of apatite (evident from the red-luminescing core of apatite in trachyte). The isotopic composition of apatite in these rocks differs markedly from all others. In the $Sr_{(i)}$ versus $\delta^{18}O$ space (Fig. 9a), they define a mixing trend from the phoscorite-carbonatite composition to more radiogenic and ^{18}O-depleted compositions. The trachyte, occurring in the form of narrow subvolcanic dikes, is most extreme, whereas the larger syenite bodies take an intermediate position (Fig. 9a). It is worth mentioning here that previously published $Sr_{(i)}$ compositions obtained on syenite (whole rock analyses; Yuhara et al. 2003, 2005) are significantly less radiogenic (0.6632–0.8850; Fig. 8). However, we question whether at the least the lower of these values can be considered probable for magmatic rocks.

The depletion in ^{18}O in apatite from trachyte and, to a lesser extent, syenite can be explained by three mechanisms: (1) involvement of ^{18}O-depleted meteoric water at moderate temperatures (above 200 °C; Deines 1989) towards the late-crystallization stage of syenitic and trachytic magmas, (2) assimilation of crustal material having experienced hydrothermal alteration (by ^{18}O-depleted meteoric fluids) prior to incorporation into the magma chamber (e.g. Riishuus et al. 2006), and (3) increased fluid-rock interaction upon cooling of a CO_2-rich deuteric fluid (e.g. Broom-Fendley et al. 2016a). Overall, the satellite bodies at Phalaborwa were emplaced at rather shallow crustal levels and the trachyte dikes at subvolcanic levels, which would have facilitated the interaction with ^{18}O-depleted meteoric fluids. Such interaction was, most likely, further enhanced by depressurizing-induced brecciation. The mixing trend with a ^{18}O-depleted, radiogenic source is, however, also explicable by various degrees of crustal contamination, as displayed by the relationship between size of intrusive body and extent of this contamination: the trachyte dikes would reflect more crustal contamination than the larger syenite bodies. Whether the source of the syenitic melts was different from that of the

main intrusive complex, as suggested by Eriksson (1982, 1989), or simply resulted from magmatic differentiation of the primary magma in the main complex (Frick 1975), cannot be finally resolved.

Processes forming apatite and its REE content

Magmatic apatite in phoscorite, carbonatite and pyroxenitic rocks

Our analyses reveal several features that are common to apatite in phoscorite, carbonatite and pyroxenitic rocks. For these three rock types, apatite has a luminescence dominated by a blue component (Figs. 3, 4), is strongly enriched in LREE (Fig. 6a–g) and does not exhibit alteration patterns that could unambiguously be interpreted as being related to late-magmatic/hydrothermal processes (such as turbid or conversion textures; Broom-Fendley et al. 2017; Zirner et al. 2015). The observed characteristics are common in primary magmatic apatite in a carbonatitic environment (e.g. Alves 2008; Broom-Fendley et al. 2016a; Decrée et al. 2015, 2016; Hayward and Jones 1991; Waychunas 2002). Our new data support Milani et al. (2017) notion that partitioning of the (L)REE in apatite in phoscorite and carbonatite at Phalaborwa is mostly due to igneous processes. The REE data obtained in this study are overall close to REE patterns of apatite from Phalaborwa published previously (Fig. 6a-d), even if a lower REE content of apatite in phoscorite must be noted in our samples (Fig. 6a).

At Phalaborwa, zonations, overgrowths, embayments and alteration zones are frequently observed in apatite under CL, especially using spectral imaging of Nd-activation. They are interpreted as magmatic in origin. Two major evolution trends regarding the distribution of REE in apatite have been revealed and further confirmed by LA-ICPMS analyses:

(1) An overall decrease in REE content is observed during apatite deposition in phoscorite, pyroxenitic rocks, and, to a lesser extent, carbonatite. This is evidenced by zoned apatite hosted by pyroxenitic rocks: the inner part of the grains is more strongly activated by Nd and, accordingly, is enriched in REE compared to its outer rim (Fig. 3b,e and Fig. 6e). Similar observations could be made on overgrowths that largely developed after abrasion/resorption of early apatite, either in its corroded rim (Fig. 4e) or inside corrosion/dissolution embayments (Fig. 3c,d). These overgrowths have a CL that is less activated by Nd than in earlier apatite (Figs. 3b,d,g and 4a) and their REE concentration is consistently lower (Fig. 6a,c,d,f). Similarly, the blue-violet CL of the early-formed massive apatite in veins is systematically more activated by Nd and the apatite is richer in REE compared to the later, dark blue/green-luminescent apatite (Figs. 3e, 4a and 6a).

Quantitative modeling of such a decrease in REE from early to later-formed apatite (in the form of crystal rims/outer zones, as overgrowths or in clusters) is difficult because partition coefficient values between apatite and different liquids (parents to the carbonatite, phoscorite, pyroxenite) are not well known. Furthermore, such modeling requires an estimate of the relative proportion of apatite in the crystallizing assemblage that cannot be constrained. However, we offer some considerations. The only simplifying issue is that all other probable major minerals (calcite, clinopyroxene and mica) co-crystallizing with apatite have very low partition coefficients. Thus, for example, the partition coefficients of REE between apatite and calcite, apatite and clinopyroxene and apatite and biotite are in the range 20–300, 50–200 and 100, as shown by Eby (1975). Hence, the values between those minerals and any liquids will be extremely small. Their crystallization will cause an increase in concentration in evolving liquids, but has essentially no effect on REE ratios such as $(La/Yb)_N$. However, if there are fundamental differences for the partition coefficients for La and Yb into apatite (and are significantly greater than unity) crystallization of apatite will affect this ratio. In the samples investigated here, the apatite partition coefficient would have to be high enough and/or the proportion of apatite great enough to produce the overall decrease in REE content of the residual melt, hindering changes of the residual melt chemistry induced by the precipitation of coexisting minerals.

The hypothesis of a progressive decrease of REE content in residual melt implies that the system was closed (at least locally, in residual melt pockets), without any further input of REE. This is also confirmed by the Sr isotope composition of apatite, which did not change in the course of apatite crystallization. By contrast, the decrease in REE is accompanied by a slight increase of the $\delta^{18}O$ values (typically below 1 ‰, occasionally up to 1.8 ‰, Figs. 7 and 9b). Such a change towards higher $\delta^{18}O$ ratios is usually ascribed to one or more of four mechanisms in carbonatitic environments: (1) sediment assimilation, (2) low-temperature alteration, (3) Rayleigh fractionation, and (4) degassing (e.g. Broom-Fendley et al. 2016a; Demeny et al. 2004). In the system considered here, and given that apatite is not readily affected by extended dissolution/reprecipitation process and volume diffusion at low temperature (typically below 550 °C; Cole and Chakraborty 2001), Rayleigh fractionation through the removal of early apatite (and possibly associated silicates) incorporating preferentially lighter O appears the most viable process to explain the slight increase in $\delta^{18}O$ in crystal rims and apatite overgrowths. Nevertheless, considering that oxygen diffusion during post-crystallization cooling (even below the closure temperature of apatite) could induce an

isotopic re-equilibration of apatite (Haynes et al. 2003), the possible role of this process should be more carefully investigated. While oxygen from the phosphate site is not susceptible to isotopic re-equilibration when interacting at lower temperature (e.g. Broom-Fendley et al. 2016a and references therein), oxygen in the hydroxyl site is more likely to substitute and exchange (Farver and Giletti 1989). In the apatite investigated, the very low amount of oxygen in the hydroxyl site (estimated at about 1.5% of the total oxygen in the apatite structure) implies that the fractionation between $\delta^{18}O$ at the OH site and in the rest of the apatite structure must be substantial to modify the O isotope signature of the bulk mineral (as already suggested for hydroxylapatite; Fortier and Lüttge 1995). A significant change of the O isotope signature at the hydroxyl site can only be achieved if apatite exchanges with a phase that is strongly enriched in ^{18}O. The existence of such a phase is not likely in the magmatic environment considered (i.e. with little evidence of low-temperature fluid involvement). These arguments tend to suggest that diffusion process during post-crystallization cooling played a minor role in the modification of the O isotope composition of apatite at Phalaborwa.

(2) In contrast, zoned apatite in carbonatite exhibits an increasing Nd-activation under CL towards its outer rim, consistently with an increase in REE content (Figs. 4h, i and 6b). The complex zoning patterns of these crystals (illustrated in Fig. 4h,i) suggest re-equilibration of earlier-formed apatite with the magma (Chakhmouradian et al. 2017; Wu et al. 2011), likely through sub-solidus diffusion at the magmatic stage (e.g. Harlov et al. 2005; Milani et al. 2017). Similar REE enrichment is observed in fissure walls of brecciated apatite crystals hosted in the carbonatite (sample GC 814; Figs. 4f, g and 6b) and in the altered zones of apatite in the massive pyroxenite crosscut by the banded carbonatite (sample GC 1994; Figs. 3h, i and 6d). These features indicate that at least one episode of carbonatite magma intrusion induced local changes in apatite chemistry leading to REE enrichment. No major change of $\delta^{18}O$ and $Sr_{(i)}$ was associated with this process (Table 4). This demonstrates that the freshly-intruding carbonatite magma had an isotopic signature close to that of the intruded rock (in which early apatite had formed). Several generations or remobilization episodes of banded carbonatite have been recognized at Phalaborwa (Eriksson 1989). This is well-reflected by one of the samples investigated in our study (sample GC 809), in which a bright orange-luminescent carbonatite was emplaced into a dull-luminescent carbonatite (Fig. 4c). Besides, this intrusion also resulted in brecciation and dissolution/corrosion of the early-formed apatite (Fig. 4c–h), which could be partly achieved through the transport of the material by the moving magma (Chakhmouradian et al. 2017).

Another notable feature that characterizes the apatite is the negative anomaly in Eu (Eu/Eu* ~ 0.75, Table 1; Fig. 6). Such an anomaly is easily explained in igneous rocks that underwent feldspar fractionation (Chakhmouradian et al. 2017), which is likely in trachyte and syenite. Nevertheless, it remains more questionable in apatite from phoscorite, carbonatite and pyroxenitic rocks, although a negative Eu anomaly is quite frequently encountered in such rocks (e.g. Bernard-Griffiths et al. 1988; Belousova et al. 2002). In these rocks, negative Eu/Eu* is commonly attributed to either of two processes: (1) the extraction of divalent Eu (together with Y) via a high-temperature aqueous fluid evolving from the magma (Bühn et al. 2001), or (2) the competition for Eu^{2+} between the various minerals in a closed system (Eby 1975). Though a negative correlation between Y content and the intensity of Eu anomaly is observed in apatite from pyroxenitic rocks (Fig. 9c), the effect of an aqueous fluid is likely limited. Instead, the negative Eu/Eu* of apatite in these rocks would be related to the coeval formation of minerals that preferentially incorporate Eu^{2+} in their structure, such as calcite, pyroxene and phlogopite. Data published previously on Phalaborwa have shown that divalent Eu is preferentially fractionated into calcite (Dawson and Hinton 2003; Wu et al. 2011) and phlogopite (Milani et al. 2017) rather than into apatite. Similarly, preferential incorporation of Eu^{2+} into pyroxene and mica has been demonstrated for the Oka Complex (Eby 1975). Preferential partitioning of Eu^{2+} into minerals formed in association with apatite in pyroxenitic rocks is also likely to explain the negative anomaly observed (Fig. 6d–g), the process being superimposed onto interactions with hot aqueous fluids.

Fluid-resetting of apatite in fenite, syenite and trachyte

Apatite in fenite, syenite and trachyte significantly differs from that in phoscorite, carbonatite and pyroxenitic rocks. In the fenite, apatite is blue-luminescent, with a green-luminescent alteration pattern (Fig. 5a). A thin Nd-activated outer rim is observed (Fig. 5b) and is locally overlain by a non-luminescing apatite associated with fluorbritholite (Fig. 5c). Most of the grain is characterized by a MREE-rich pattern with a negative Eu anomaly (Fig. 6h), which has been reported from apatite in other fenitized/metasomatised rocks (e.g. Broom-Fendley et al. 2017; Krneta et al. 2018; Zirner et al. 2015). A slight depletion in LREE superimposed onto this pattern highlights the alteration leading to the green-luminescent apatite deposition (Fig. 6h). The decrease in LREE in apatite is commonly attributed to mobilization of these elements during fluid flow through the rock (e.g. Harlov et al. 2002; Krneta et al. 2018; Li and Zhou 2015). The

lack of significant changes in the O and Sr isotope compositions in the different zones of the grain (Figs. 7 and 8) implies that the fluid(s) involved in alteration was (were) probably isotopically close to the metasomatic fluid from which the early-formed apatite crystallized. The assemblage of non-luminescent apatite and fluorbritholite would have formed at the expense of this REE-rich apatite, via coupled substitution and mass transfer (Giebel et al. 2017).

In the syenite, apatite displays a complex turbid texture under CL (Fig. 5d), which indicates late-magmatic/hydrothermal processes (Broom-Fendley et al., 2016b). This alteration led to a slight leaching of LREE and enrichment in M/HREE of the green-luminescent altered rim of the crystal compared to the blue-greenish luminescent core (Fig. 5d and Fig. 6h). As for fenite, these geochemical features can be explained by the preferential mobilization of LREE through fluid-rock interactions (e.g. Harlov et al. 2002). In addition, formation of this apatite was associated with an increase in $Sr_{(i)}$ and a decrease in $\delta^{18}O$ (Fig. 9a,d,e; Table 4). One can argue that these changes point to increasing involvement of $\delta^{18}O$-depleted meteoric water (as explained in "New insights into magmatic processes and sources at Phalaborwa" above) and contribution from/interaction with the country rocks during late stages of syenite magma emplacement.

Apatite hosted by trachyte is zoned and the transition between the growth bands is gradational (Fig. 5f): the reddish-brown (due to a mix between red, green CL colors, with some hints of blue) luminescent core is overgrown by blue-luminescent apatite, which is in turn overlain by green-luminescent apatite (Fig. 5f). A zoning pattern that evolves from a red/green towards a blue luminescence over time is common in apatite growing in carbonatitic environments (e.g. Alves 2008; Decrée et al. 2016; Hayward and Jones 1991; McLemore and Barker 1987). The increase in MREE and HREE noted during the continuous growth of apatite (Fig. 6i) would indicate that no mineral capable of concentrating HREE and subsequently preventing apatite from scavenging HREE (Cao et al. 2012; Chu et al. 2009) formed during magma differentiation. Increasing interaction with meteoric water and the country rocks (see "New insights into magmatic processes and sources at Phalaborwa") is the best explanation for the decrease in $\delta^{18}O$ and progressive enrichment in radiogenic Sr observed from the core to the rim of this apatite (Fig. 9a,c,d). Fluid- or magma-rock interaction during trachyte emplacement could explain the slight depletion in LREE of the green-luminescent rim, as the alteration patterns observed in apatite. Similar forms of alteration occurring at all stages of apatite crystallization have been described in the carbonatite complex at Otjisazu (Bühn et al. 2001) and in the Ilímaussaq complex (Zirner et al. 2015).

Summary and conclusions

This petrological, mineral-chemical and in-situ isotope (Sr and O) study focused on the processes that led to the formation of apatite in a large variety of rocks at Phalaborwa and which controlled the distribution of REE in this mineral. In phoscorite, carbonatite and pyroxenitic rocks, apatite formation mainly resulted from igneous processes, as evidenced by its typical blue-violet CL and LREE enrichment, and lack of alteration textures. In phoscorite and pyroxenitic rocks, crystallization of apatite was marked by a moderate decrease in REE and a slight increase in $\delta^{18}O$, with unchanged $Sr_{(i)}$. These changes can be explained by Rayleigh fractionation, in relation with magma differentiation and early apatite fractionation in isolated interstitial melt pockets. By contrast, in carbonatite, secondary REE enrichment of early-formed apatite is due to re-equilibration of the latter through subsolidus diffusion at the magmatic stage with a fresh carbonatite magma intruding already existing carbonatite. In the fenite, syenite and trachyte, fluid-rock/magma interactions are evidenced at various stages of apatite crystallization by alteration textures. Alteration by fluid also induced leaching of LREE from apatite.

Our new isotope data highlight the predominant role of magmatic processes in the distribution of REE in apatite from the rock types hosting the phosphate mineralization at Phalaborwa. It also confirms the independent formation of pyroxenitic rocks compared to phoscorite and carbonatite, the latter two having a common genetic origin. Finally, the new data acquired on apatite give clues about the formation of the satellite bodies in the complex (i.e. their epizonal emplacement and interaction of the syenitic magma with meteoric waters and the substratum).

Regarding the methodology for fingerprinting purposes, this study emphasized that the spectral CL of the Nd^{3+} emission at 880 nm is a powerful tool to quickly reveal REE distribution and enrichment in apatite as well as enhancing crystal textures. It reflects with great sensitivity the chemical evolution of apatite through time. Combined CL, LA-ICPMS and in-situ O and Sr isotope compositions are helpful to decipher enrichment processes and investigate the question of element/fluid source at the scale of the complex. In future, it will be worth using these tools more systematically to study apatite in alkaline complexes.

Acknowledgements The authors would like to express their gratitude to Ulrich Schüssler and Stefan Höhn for assistance in acquiring electron microprobe analyses at the University of Würzburg. Samples were provided by Grant Cawthorn who gratefully acknowledges the hospitality of the management and geological staff at Foskor (Pty) Ltd for many repeated student excursions to their property. The LA-ICP-MS laboratory from GeoRessources was partly funded by the French National Research Agency through the national program "Investissements d'avenir" of the Labex Ressources21 with the reference

ANR-10-LABX-21-RESSOURCES21. The authors are also grateful to Daniela Rubatto (Associate Editor), Sam Broom-Fendley (Reviewer) and an anonymous reviewer, for helpful remarks on the manuscript. Their comments have contributed to improve substantially the quality of this paper.

References

Alves PR (2008) The carbonatite-hosted apatite deposit of Jacupiranga, SE Brazil: Styles of mineralization, ore characterization, and association with mineral processing. Unpublished PhD thesis, Missouri University of Science and Technology

Baele JM, Decrée S, Rusk B (2019) Cathodoluminescence applied to ore geology and exploration. In: Decrée S, Robb L (eds) Ore deposits: Origin, exploration, and exploitation. Wiley, New York, pp 131–161

Belousova EA, Griffin WL, O'Reilly SY, Fisher NI (2002) Apatite as an indicator mineral for mineral exploration: trace-element compositions and their relationship to host rock type. J Geochem Explor 76:45–69

Bernard-Griffiths J, Peucat JJ, Fourcade S, Kienast JR, Ouzegane K (1988) Origin and evolution of 2 Ga old carbonatite complex (Ihouhaouene, Ahaggar, Algeria): Nd and Sr isotopic evidence. Contrib Miner Petrol 100:339–348

Blanc P, Baumer A, Cesbron F, Ohnenstetter D, Panczer G, Rémond G (2000) Systematic cathodoluminescence spectral analysis of synthetic doped minerals: anhydrite, apatite, calcite, fluorite, scheelite and zircon. In: Pagel M, et al. (eds) Cathodoluminescence in Geosciences. Springer Verlag, New York, pp 127–160

Broom-Fendley S, Heaton T, Wall F, Gunn G (2016a) Tracing the fluid source of heavy REE mineralisation in carbonatites using a novel method of oxygen-isotope analysis in apatite: the example of Songwe Hill, Malawi. Chem Geol 440:275–287

Broom-Fendley S, Styles MT, Appleton JD, Gunn G, Wall F (2016b) Evidence for dissolution-reprecipitation of apatite and preferential LREE mobility in carbonatite-derived late-stage hydrothermal processes. Am Miner 101:596–611

Broom-Fendley S, Brady AE, Wall F, Gunn G, Dawes W (2017) REE minerals at the Songwe Hill carbonatite, Malawi: HREE-enrichment in late-stage apatite. Ore Geol Rev 81:23–41

Buchholz P, Foya S (2015) Investor's and Procurement Guide South Africa, DERA. Rohstoffinformationen 22 Deutsche. Rohstoffagentur, Berlin

Bühn B, Dörr W, Brauns CM (2001) Petrology and age of the Otjisazu carbonatite complex, Namibia: implications for the pre-and syn-orogenic Damaran evolution. J Afr Earth Sci 32:1–17

Cao M, Li G, Qin K, Seitmuratova EY, Liu Y (2012) Major and trace element characteristics of apatites in granitoids from Central Kazakhstan: implications for petrogenesis and mineralization. Res Geol 62:63–83

Chakhmouradian AR, Reguir EP, Zaitsev AN et al (2017) Apatite in carbonatitic rocks: Compositional variation, zoning, element partitioning and petrogenetic significance. Lithos 274:188–213

Chen J, Shen SZ, Li XH et al (2016) High-resolution SIMS oxygen isotope analysis on conodont apatite from South China and implications for the end-Permian mass extinction. Palaeogeogr Palaeoclim Palaeoecol 448:26–38

Chu MF, Wang KL, Griffin WL et al (2009) Apatite composition: tracing petrogenetic processes in Transhimalayan granitoids. J Petrol 50:1829–1855

Cole DR, Chakraborty S (2001) Rates and mechanisms of isotopic exchange. Rev Miner Geochem 43:83–223

Conway CM, Taylor HP Jr (1969) O^{18}/O^{16} and C^{13}/C^{12} ratios of coexisting minerals in the Oka and Magnet Cove carbonatite bodies. J Geol 77:618–626

Dawson JB, Hinton RW (2003) Trace-element content and partitioning in calcite, dolomite and apatite in carbonatite, Phalaborwa, South Africa. Miner Mag 67:921–930

Deans T (1966) Economic mineralogy of African carbonatites. In: Tuttle OF, Gittins J (eds) Carbonatites, Interscience. Wiley, New York, pp 385–413

Decrée S, Boulvais P, Cobert C et al (2015) Structurally-controlled hydrothermal alteration in the Upper Ruvubu Alkaline Plutonic Complex (Burundi): implications for REE and HFSE mobilities. Precambr Res 269:281–295

Decrée S, Boulvais P, Tack L, André L, Baele JM (2016) Fluorapatite in carbonatite-related phosphate deposits: the case of the Matongo carbonatite (Burundi). Miner Dep 51:453–466

Deines P (1989) Stable isotope variations in carbonatite. In: Bell K (ed) Carbonatites: genesis and evolution. Unwin Hyman, London

De Jager DH (1989) Phosphate resources in the Palabora igneous complex, Transvaal, South Africa. In: Notholt AJG, Sheldon RP, Davidson DF (eds) Phosphate deposits of the world. Cambridge University Press, Cambridge, pp 267–272

Demény A, Sitnikova MA, Karchevsky PI (2004) Stable C and O isotope compositions of carbonatite complexes of the Kola Alkaline Province: phoscorite-carbonatite relationships and source compositions. In: Wall F, Zaitsev A (eds) Phoscorites and carbonatites from mantle to mine: the key example of the Kola Alkaline Province. Mineralogical Society Series, Berlin, pp 407–431

De Toledo MCM, Lenharo SL, Ferrari VC, Fontan F, De Parseval P, Leroy G (2004) The compositional evolution of apatite in the weathering profile of the Catalão I alkaline-carbonatitic complex, Goiás, Brazil. Can Miner 42:1139–1158

Eby GN (1975) Abundance and distribution of the rare-earth elements and yttrium in the rocks and minerals of the Oka carbonatite complex, Quebec. Geochim Cosmochim Acta 39:597–620

Emsbo P, McLaughlin PI, Breit GN, du Bray EA, Koenig AE (2015) Rare earth elements in sedimentary phosphate deposits: Solution to the global REE crisis? Gondwana Res 27:776–785

Emo RB, Smit MA, Schmitt M et al (2018) Evidence for evolved Hadean crust from Sr isotopes in apatite within Eoarchean zircon from the Acasta Gneiss Complex. Geochim Cosmochim Acta 235:450–462

Eriksson S (1982) Aspects of the petrochemistry of the Phalaborwa Igneous Complex, northeastern Transvaal, South Africa. Unpublished PhD Thesis, University of the Witwatersrand, Johannesburg

Eriksson SC (1989) Phalaborwa: a saga of magmatism, metasomatism and miscibility. In: Bell K (ed) Carbonatites: genesis and evolution. Unwin Hyman, London, pp 221–254

Farver JR, Giletti BJ (1989) Oxygen and strontium diffusion kinetics in apatite and potential applications to thermal history determinations. Geochim Cosmochim Acta 53:1621–1631

Frick C (1975) The Phalaborwa syenite intrusions. Trans Geol Soc S Africa 78:201–213

Fortier SM, Lüttge A (1995) An experimental calibration of the temperature dependence of oxygen isotope fractionation between apatite and calcite at high temperatures (350–800 C). Chem Geol 125:281–290

Fourie PJ, De Jager DH (1986) Phosphate in the Phalaborwa complex. In: Anhaeusser CR, Maske S (eds) Mineral deposits of Southern Africa. Geological Society of South Africa, Johannesburg, pp 2239–2253

Giebel RJ, Gauert CD, Marks MA, Costin G, Markl G (2017) Multistage formation of REE minerals in the Palabora Carbonatite Complex, South Africa. Am Miner 102:1218–1233

Giebel RJ, Marks MA, Gauert CD, Markl G (2019) A model for the formation of carbonatite-phoscorite assemblages based on the

compositional variations of mica and apatite from the Palabora Carbonatite Complex, South Africa. Lithos 324:89–104
Goldoff B, Webster JD, Harlov DE (2012) Characterization of fluorchlorapatites by electron probe microanalysis with a focus on time-dependent intensity variation of halogens. Am Miner 97:1103–1115
Goodenough KM, Schilling J, Jonsson E et al (2016) Europe's rare earth element resource potential: an overview of REE metallogenetic provinces and their geodynamic setting. Ore Geol Rev 72:838–856
Götte J (2009) Petrological modifications in continental target rocks from terrestrial impact structures: Evidence from cathodoluminescence. In: Gucsik A (ed) Cathodoluminescence and its application in the planetary sciences. Springer-Verlag, Berlin, pp 45–60
Groves DI, Vielreicher NM (2001) The Phalabowra (Palabora) carbonatite-hosted magnetite–copper sulfide deposit, South Africa: an end-member of the iron-oxide copper–gold–rare earth element deposit group? Miner Dep 36:189–194
Habermann D, Neuser RD, Richter DK (2000) Quantitative high resolution spectral analysis of Mn2+ in sedimentary calcite. In: Pagel M, Barbin V, Blanc P, Ohnenstetter D (eds) Cathodoluminescence in geosciences. Springer, Heidelberg, pp 331–358
Hanekom HJ (1965) The geology of the palabora igneous complex. South Africa Geological Survey Handbook, Memoir
Harlov DE, Andersson UB, Förster HJ, Nyström JO, Dulski P, Broman C (2002) Apatite-monazite relations in the Kiirunavaara magnetite-apatite ore, northern Sweden. Chem Geol 191:47–72
Harlov DE, Wirth R, Förster HJ (2005) An experimental study of dissolution–reprecipitation in fluorapatite: fluid infiltration and the formation of monazite. Contrib Miner Petrol 150:268–286
Hayward CL, Jones AP (1991) Cathodoluminescence petrography of Middle Proterozoic extrusive carbonatite from Qasiarsuk, South Greenland. Min Mag 55:591–603
Haynes EA, Moecher DP, Spicuzza MJ (2003) Oxygen isotope composition of carbonates, silicates, and oxides in selected carbonatites: constraints on crystallization temperatures of carbonatite magmas. Chem Geol 193:43–57
Hennig-Michaeli C (1968) Mikroskopische untersuchungen an hanstucken der kupfererzlagerstatte am Loolekop im Phalaborwa Komplex, NE-Transvaal. Unpublished Master thesis, Institut fur Mineralogie und Lagerstattenlehre der RW and Aachen, Germany
Ihlen PM, Schiellerup H, Gautneb H, Skår Ø (2014) Characterization of apatite resources in Norway and their REE potential—a review. Ore Geol Rev 58:126–147
Heinrich EW (1970) The Palabora carbonatitic complex; a unique copper deposit. Can Miner 10:585–598
Kempe U, Götze J (2002) Cathodoluminecence (CL) behaviour and crystal chemistry of apatite from rare-metal deposits. Min Mag 66:151–172
Krneta S, Ciobanu C, Cook N, Ehrig K (2018) Numerical modeling of REE fractionation patterns in fluorapatite from the Olympic Dam Deposit (South Australia). Minerals 8:342
Jackson WD, Christiansen G (1993) International strategic minerals inventory summary report-rare-earth Oxides. US Government Printing Office, Washington, p 930
Jochum KP, Weis U, Stoll B et al (2011) Determination of reference values for NIST SRM 610–617 glasses following ISO guidelines. Geostand Geoanal Res 35:397–429
Li X, Zhou MF (2015) Multiple stages of hydrothermal REE remobilization recorded in fluorapatite in the Paleoproterozoic Yinachang Fe–Cu–(REE) deposit, Southwest China. Geochim Cosmochim Acta 166:53–73
Li Z, Duan D, Jiang S, Ma Y, Yuan H (2018) In situ analysis of major elements, trace elements and Sr isotopic compositions of apatite from the granite in the Chengchao skarn-type Fe deposit, Edong ore district: Implications for petrogenesis and mineralization. J Earth Sci 29:295–306
Lombaard AF, Ward-Able NM, Bruce RW (1964) The exploration and main geological features of the copper deposit in carbonatite at Loolekop, Palabora complex. Geol Some Ore Dep S Afr 2:315–337
Longerich HP, Jackson SE, Günther D (1996) Inter-laboratory note. Laser ablation inductively coupled plasma mass spectrometric transient signal data acquisition and analyte concentration calculation. J Anal At Spectrom 11:899–904
Mariano AN (1989) Nature of economic mineralization in carbonatites and related rocks. In: Bell K (ed) Carbonatites: genesis and evolution. Unwin Hyman, London, pp 149–176
Mariano AN, Mariano A (2012) Rare earth mining and exploration in North America. Elements 8:369–376
Marks MA, Wenzel T, Whitehouse MJ et al (2012) The volatile inventory (F, Cl, Br, S, C) of magmatic apatite: an integrated analytical approach. Chem Geol 291:241–255
Marshall DJ (1988) Cathodoluminescence of geological materials. Hyman, Boston, 146 p
McDonough WF, Sun SS (1995) The composition of the Earth. Chem Geol 120:223–253
McLemore VT, Barker JM (1987) Some geological application of cathodoluminescence, examples from the Lemitar Mountains and Riley travertine, Socorro County, New Mexico. New Mexico Geology, 37–40
Milani L, Bolhar R, Frei D, Harlov DE, Samuel VO (2017) Light rare earth element systematics as a tool for investigating the petrogenesis of phoscorite-carbonatite associations, as exemplified by the Phalaborwa Complex, South Africa. Miner Dep 52:1105–1125
Orris GJ, Chernoff CB (2002) Data set of world phosphate mines, deposits, and occurrences: Part B Location and mineral economic data. US Department of the Interior, US Geological Survey, Reston
Pan Y, Fleet ME (2002) Compositions of the apatite-group minerals: substitution mechanisms and controlling factors. Rev Miner Geochem 48:13–49
Paton C, Hellstrom J, Paul B, Woodhead J, Hergt J (2011) Iolite: Freeware for the visualisation and processing of mass spectrometric data. J Anal At Spectrom 26:2508–2518
Pell J (1996) Mineral deposits associated with carbonatites and related alkaline igneous rocks. In: Mitchell RH (ed) Undersaturated alkaline rocks: Mineralogy, petrogenesis, and economic potential. Short course series. Mineralogical Association of Canada, Winnipeg, pp 271–310
Pineau F, Javoy M, Allegre CJ (1973) Etude systematique des isotopes de l'oxygene, du carbone et du strontium dans les carbonatites. Geochim Cosmochim Acta 37:2363–2377
Potts PJ, Tindle AG (1989) Analytical characteristics of a multilayer dispersion element (2d=60Å) in the determination of fluorine in minerals by electron microprobe. Miner Mag 53:357–362
Reischmann T (1995) Precise U/Pb age determination with baddeleyite (ZrO2), a case study from the Phalaborwa igneous complex, South Africa. S Afr J Geol 98:1–4
Riishuus MS, Peate DW, Tegner C, Wilson JR, Brooks CK, Harris C (2006) Temporal evolution of a long-lived syenitic centre: the Kangerlussuaq Alkaline Complex, East Greenland. Lithos 92:276–299
Rudashevsky NS, Kretser YL, Rudashevsky VN, Sukharzhevskaya ES (2004) A review and comparison of PGE, noble-metal and sulphide mineralization in phoscorites and carbonatites from Kovdor and Phalaborwa. In: Wall F, Zaitsev A (eds) Phoscorites and carbonatites from mantle to mine: the key example of the Kola Alkaline Province, Mineralogical Society Series 10, pp 375–405
Roux EH, Goodey JG, Wepener EF, Hodierne KR (1989) Phosphate in South Africa. J S Afr Inst Min Metal 89:129–139

Santos RV, Clayton RN (1995) The carbonate content in high-temperature apatite: an analytical method applied to apatite from the Jacupiranga alkaline complex. Am Miner 80:336–344

Stormer JC, Pierson ML, Tacker RC (1993) Variation of F and Cl X-ray intensity due to anisotropic diffusion in apatite during electron microprobe analysis. Am Miner 78:641–648

Suwa K, Oana S, Wada H, Osaki S (1975) Isotope geochemistry and petrology of African carbonatites. Elsevier, Pergamon, pp 735–745

Sun Y, Wiedenbeck M, Joachimski MM, Beier C, Kemner F, Weinzierl C (2016) Chemical and oxygen isotope composition of gem-quality apatites: implications for oxygen isotope reference materials for secondary ion mass spectrometry (SIMS). Chem Geol 440:164–178

Taylor HP, Frechen J, Degens ET (1967) Oxygen and carbon isotope studies of carbonatites from Laacher See district, West Germany and Alnø district, Sweden. Geochim Cosmochim Acta 31:407–430

Tichomirowa M, Grosche G, Götze J, Belyatsky BV, Savva EV, Keller J, Todt W (2006) The mineral isotope composition of two Precambrian carbonatite complexes from the Kola Alkaline Province-Alteration versus primary magmatic signatures. Lithos 91:229–249

Trotter JA, Williams IS, Barnes CR, Lécuyer C, Nicoll RS (2008) Did cooling oceans trigger Ordovician biodiversification? Evidence from conodont thermometry. Science 321:550–554

Vartiainen H, Paarma H (1979) Geological characteristics of the Sokli Carbonatite Complex, Finland. Econ Geol 74:1296–1306

Verwoerd WJ, Du Toit MC (2006) The Phalaborwa and Schiel complexes. In: Johnson MR, et al. (eds) The geology of South Africa. Council for Geosciences, Pretoria, pp 291–318

Walter AV, Nahon D, Flicoteaux R, Girard JP, Melfi A (1995) Behaviour of major and trace elements and fractionation of REE under tropical weathering of a typical apatite-rich carbonatite from Brazil. Earth Planet Sci Lett 136:591–602

Waychunas GA (2002) Apatite luminescence. In: Kohn MJ, Rakovan J, Hughes JM (eds) Reviews in mineralogy and geochemistry, vol 48. Phosphates Mineralogical Society of America, Washington, pp 701–742

Wu FY, Yang YH, Li QL, Mitchell RH, Dawson JB, Brandl G, Yuhara M (2011) In situ determination of U-Pb ages and Sr–Nd–Hf isotopic constraints on the petrogenesis of the Phalaborwa carbonatite complex, South Africa. Lithos 127:309–322

Yang YH, Wu FY, Yang JH et al (2014) Sr and Nd isotopic compositions of apatite reference materials used in U-Th–Pb geochronology. Chem Geol 385:35–55

Yang JH, Kang LF, Peng JT, Zhong H, Gao JF, Liu L (2018) In situ elemental and isotopic compositions of apatite and zircon from the Shuikoushan and Xihuashan granitic plutons: Implication for Jurassic granitoid-related Cu-Pb-Zn and W mineralization in the Nanling Range, South China. Ore Geol Rev 93:382–403

Yuhara M, Kohno M, Kagami H, Hiroi Y, Tsuchiya N (2003) Geochemistry of syenite of the Phalaborwa carbonatite complex, South Africa. Polar Geosci 16:176–195

Yuhara M, Hirahara Y, Nishi N, Kagami H (2005) Rb-Sr, Sm-Nd ages of the phalaborwa carbonatite complex, South Africa. Polar Geosci 18:101–113

Zeng LP, Zhao XF, Li XC, Hu H, McFarlane C (2016) In situ elemental and isotopic analysis of fluorapatite from the Taocun magnetite-apatite deposit, Eastern China: Constraints on fluid metasomatism. Am Miner 101:2468–2483

Zhao XF, Zhou MF, Gao JF, Li XC, Li JW (2015) In situ Sr isotope analysis of apatite by LA-MC-ICPMS: constraints on the evolution of ore fluids of the Yinachang Fe-Cu-REE deposit, Southwest China. Miner Dep 50:871–884

Zigaitė Z, Whitehouse M (2014) Stable oxygen isotopes of dental biomineral: differentiation at the intra-and inter-tissue level of modern shark teeth. GFF 136:337–340

Zirner AL, Marks MA, Wenzel T, Jacob DE, Markl G (2015) Rare earth elements in apatite as a monitor of magmatic and metasomatic processes: The Ilímaussaq complex, South Greenland. Lithos 228:12–22